Stochastic reconstruction of 3D microstructures from 2D cross-sectional images using machine learning-based characterization

Jinlong Fu[a], Dunhui Xiao[a], Dongfeng Li[b], Hywel R. Thomas[a], and Chenfeng Li *[a,c]

[a]Zienkiewicz Centre for Computational Engineering, College of Engineering, Swansea University Bay Campus, Swansea SA1 8EN, United Kingdom
[b]School of Science, Harbin Institute of Technology - Shenzhen, Shenzhen, China
[c]Energy Safety Research Institute, College of Engineering, Swansea University Bay Campus, Swansea SA1 8EN, United Kingdom

Abstract

The availability of high-quality three-dimensional (3D) microstructures is an essential prerequisite to understanding the macroscopic behaviours of heterogeneous media. Considering the high cost of 3D microscopy imaging, it is an economical way to derive large numbers of virtual 3D microstructures from limited morphological information of 2D cross-sectional images. This paper presents an efficient method that incorporates machine learning-based characterization of 2D images to statistically reconstruct 3D microstructures. The latent stochasticity of 2D images is mastered by fitting supervised machine learning models, which essentially characterize the local morphological statistics. A morphology integration scheme is developed to project the 2D morphological statistics into the 3D space, and new equivalent 3D microstructures can then be synthesized by sequentially generating voxel values from probability sampling. The new method is tested on a series of heterogeneous media with distinct morphologies, and it is also compared with two classical methods (i.e. stochastic optimization-based reconstruction and Gaussian random field transformation) in terms of reconstruction accuracy and efficiency. Besides, various microstructural descriptors are used to quantify the discrepancies between the reconstructed and target microstructures. The results confirm that the proposed method provides a highly cost-effective and widely applicable way to reproduce 3D realizations that precisely preserve the statistical characteristics, geometrical irregularities, long-distance connectivity and anisotropy that exist in 2D cross-sectional images.

Keywords: Random heterogeneous media; Stochastic reconstruction; Machine learning-based characterization; Statistical equivalence; Microstructural descriptors.

1 Introduction

Macroscopic behaviours of a random heterogeneous medium are intrinsically linked to its microstructural characteristics, and they usually exhibit strong stochasticity and uncertainty, due to the random spatial distributions of different material components (Torquato, 2013). Accurate characterization (Anovitz and Cole, 2015; Bultreys et al., 2016) of the internal microstructure is an essential prerequisite for successful modelling of effective material properties (i.g. mechanical, transport and conductive properties). Advanced microscopy imaging techniques, such as micro-CT (Schlüter et al., 2014) and FIB-SEM (Blunt et al., 2013), are capable to directly provide high-resolution 3D datasets of heterogeneous microstructures, but such 3D characterization is often limited to small volume measurements that are insufficient in terms of representative significance. Compared to 3D image acquisition, it is much cheaper and easier to achieve high-quality 2D characterization of representative elementary volume (REV) from SEM (Stutzman, 2004), BSE (Scrivener, 2004) or other microscopy devices, by only inuring one-hundredth (even one-thousandth) of cost and effort. In many cases, only 2D thin sections are available, but

---

[*] Corresponding author: c.f.li@swansea.ac.uk

3D microstructural informatics is still essential to analyse the microstructure-property relationships, especially for numerical simulation, computational design and performance prediction. An attractive and economical way to deal with this problem is to infer realistic 3D microstructures from the available 2D cross-sectional images by preserving the statistical equivalence and microstructural complexities.

Over the past few decades, extensive efforts have been made on stochastic microstructure reconstruction. Generally, stochastic optimization-based reconstruction (SOR) (Torquato and Yeong, 1998; Ju et al., 2014; Karsanina and Gerke, 2018) and Gaussian random field transformation (GRFT) (Liang et al., 1998; Feng et al., 2014, 2016) are the most widely-used methods to derive 3D microstructures from 2D reference images. However, the accuracy of SOR strongly depends on the predefined optimization objective(s), and the iterative nature also makes it extremely time-consuming and computation-intensive. Although GRFT can generate microstructure samples instantly through field transformation and level truncation, the captured low-order information is far from sufficient to preserve microstructural complexity and heterogeneity. Besides, other reconstruction methods, such as multiple-point statistics method (Okabe and Blunt, 2005; Hajizadeh et al., 2011; Wu et al., 2018), Markov Chain Monte Carlo simulation (Wu et al., 2006), continuum reconstruction (Latief et al., 2010), patch-based method (Tahmasebi and Sahimi, 2012), texture synthesis method (Liu and Shapiro, 2015; Turner and Kalidindi, 2016) and other methods (Yang et al., 2018), are also popular in some specific areas. The effectiveness of a stochastic microstructure reconstruction method depends on its accuracy and efficiency, from which a large number of statistically, geometrically and topologically realistic samples should be quickly generated to form a complete computation ensemble covering all possible configurations. The newly reconstructed 3D microstructure samples can then be used to analyze the physical properties of heterogeneous materials or porous media through various research approaches, such as numerical simulation (Golparvar et al., 2018; Ijeje et al., 2019; Fu et al., 2020a,b) and data-driven or physics-informed machine learning (Wood, 2018; Choubineh et al., 2019; Li et al., 2019; Yang et al., 2021; Fu et al., 2021b; Shukla et al., 2021).

With the rapid growth of artificial intelligence techniques and associated applications in recent years, various machine/deep learning algorithms have been applied to microstructural property analysis. Support vector machine (Sundararaghavan and Zabaras, 2005), decision tree (Bostanabad et al., 2016a,b), deep belief network (Cang et al., 2017), generative adversarial network (Mosser et al., 2017; Feng et al., 2020), convolutional neural network (Li et al., 2018; Wang et al., 2018), transfer learning (Bostanabad, 2020), stacked sparse autoencoder (Fu et al., 2021a) and hybrid deep learning model (Zhang et al., 2021) have been used to generate random heterogeneous microstructures by preserving complicated morphologies. However, the use of complicated machine learning models in microstructure reconstruction often greatly increases the computational intensity and raises the memory requirement. Large prior datasets of training images are usually demanded to feed the complicated learning models, which is often unavailable in practice. Besides, most machine/deep learning-based methods are developed for equidimensional (2D-to-2D or 3D-to-3D) reconstruction, instead of dimensionally-upgraded (2D-to-3D) reconstruction. As a result, it remains a challenging task to develop an accurate and efficient reconstruction method that can create statistically equivalent and morphologically realistic 3D microstructures from 2D cross-sectional images.

Inspired by the multiple-point statistics method (MPSM) (Okabe and Blunt, 2005; Hajizadeh et al., 2011; Wu et al., 2018) and the supervised learning-based method (SLM) (Bostanabad et al., 2016a,b; Fu et al., 2021a), we developed a novel 2D-to-3D microstructure reconstruction method by combining the advantages of both SLM and MPSM. The original SLM focuses on equidimensional reconstruction, but its idea of using supervised machine learning to statistically characterize heterogeneous microstructures is borrowed in this work. The proposed method adopts artificial neural networks (ANN) with a shallow architecture to learn the inherent stochasticity from the 2D training image(s) in a supervised learning paradigm, and then the 2D statistical characteristics stored in the fitted ANN model(s) are projected to 3D space through a specially designed scheme of information integration, based on which 3D microstructure samples can be synthesized via sequential probability sampling. Due to the powerful ability of machine learning in data analysis, the proposed method is more capable than the MPSM in characterizing microstructural complexities, such as low volume fraction, geometrical irregularity, wide-range pore size, long-distance connectivity and anisotropy. Different from other deep/machine learning-based methods that require large training datasets, the proposed method achieves accurate characterization of microstructural complexities by using only several (or even one) representative 2D images. Besides, the proposed method is also much easier to implement and more convenient for practical applications, because many supervised learning algorithms are readily available off-the-shelf, which can be directly used for the microstructure reconstruction purpose.

To demonstrate the performance of the new method, a series of 2D-to-3D reconstruction tests are conducted on different microstructures with diverse morphologies, and the reconstruction results are later compared with two classic methods: SOR and GRFT, in terms of reconstruction accuracy and efficiency. These tests demonstrate that the new method can efficiently generate 3D samples that preserve the statistical equivalences, morphological similarities, geometrical irregularities and topological attributes of the original microstructures. The rest of the paper is organized as follows. § 2 explains the supervised machine learning-based characterization of microstructural complexities, including basic theory, training data collection and ANN model construction. § 3 gives a detailed account of the 3D microstructure reconstruction procedure by using the 2D statistical characteristics stored in the pretrained supervised machine learning model(s). In § 4, a series of testing examples are used to demonstrate the remarkable superiority and general applicability of the proposed method on 2D-to-3D microstructure reconstruction. Finally, concluding remarks are made in § 5, to discuss the strengths and weaknesses of the new method and summarise the main contributions of this study.

2 Machine learning-based characterization of 2D cross-sectional images

In this section, we take a bi-phase microstructure as an example to explain how to statistically characterize microstructural complexities via supervised machine learning. After image acquisition from microscopy devices, the raw scanning image will be processed and segmented into a discrete form, where different material components are separated from each other, permitting subsequent analyses such as quantitative characterization and numerical simulation. As shown in Figure 1, a 2D slice of micro-CT scanning image is segmented into a binary image with white and black phases. In computer vision, a 2D digital image is a data structure that represents a generally rectangular grid of pixels (Soille, 2013), and a 2D matrix $\boldsymbol{X}$ can be used to represent the bi-phase microstructure as follows:

$$X(i,j) = X_{ij} = \begin{cases} 1, & \text{if } (i,j) \text{ is located at white phase,} \\ 0, & \text{if } (i,j) \text{ is located at black phase.} \end{cases} \tag{1}$$

where X_{ij} is the binary pixel value, and i and j denote the position of this pixel in the 2D image (namely, they are the indexes of row and column in the 2D matrix, respectively.)

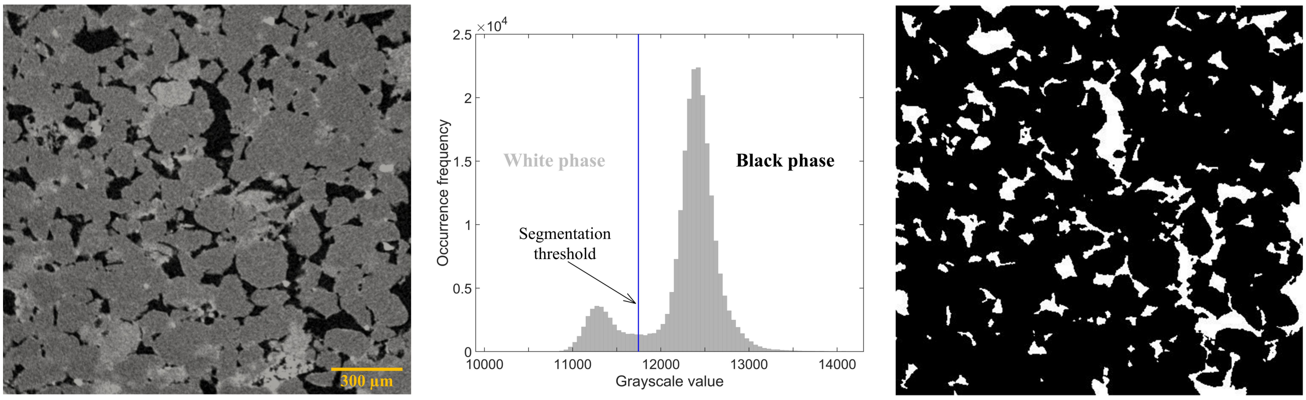

(a) (b) (c)

Figure 1: Illustration of image segmentation: (a) A 2D slice of the micro-CT image of a Leopard sandstone sample, where the pore space is shown in dark; (b) The histogram of the grayscale values, based on which the segmentation threshold is determined; and (c) The binary image with two distinct phases, where the white phase denotes the pore space and the black phase denotes the solid matrix.

2.1 Markov random field assumption

Due to the stochastic nature of heterogeneous media, the matrix $\boldsymbol{X}$ corresponding to a microstructure sample can be considered as a random realization from the underlying full joint probability distribution function (PDF) $p(\boldsymbol{X})$ or $p(X_{11}, X_{12}, ..., X_{ij}, ...)$. Although $p(\boldsymbol{X})$ is the ideal statistical measure to characterize the microstructure $\boldsymbol{X}$, its extremely high dimension hampers the direct computation from limited digital image samples (Fu et al., 2021a; Wang et al., 2021). To simplify the problem and enable statistical computation, heterogeneous microstructures are often mathematically modelled as Markov random fields (MRFs) (Okabe and Blunt, 2005; Hajizadeh et al., 2011; Liu and Shapiro, 2015; Turner and Kalidindi, 2016; Bostanabad et al., 2016a; Fu et al., 2021a).

In image analysis, MRF has been proved to be a remarkably successful tool to model various image textures, where image textures are assumed to be random processes with locality and stationarity properties (Wei and Levoy, 2000; Li, 2009). The locality property states that the value of a pixel X_{ij} in the image $\boldsymbol{X}$ is only related to its neighbouring pixels $\mathbf{N}_{ij}$ and independent of all other pixels beyond this neighbourhood area, which can be mathematically expressed by the relationship between conditional PDFs:

$$p(X_{ij}|\mathbf{X}^{(-ij)}) = p(X_{ij}|\mathbf{N}_{ij}) \tag{2}$$

where $\mathbf{X}^{(-ij)}$ denotes the rest of pixels in $\boldsymbol{X}$ excluding X_{ij}. The stationarity property states that different local regions $LR(X_{ij}, \mathbf{N}_{ij})$ inside the image $\boldsymbol{X}$ always share the same statistical characteristics. In general, the neighbouring range should be large enough to cover the basic features of microstructures. Obviously, the local region $LR(X_{ij}, \mathbf{N}_{ij})$ has a much lower dimension compared to the entire image $\boldsymbol{X}$. Therefore, it is an attractive and practical way to compute the local conditional PDF (CPDF) $p(X_{ij}|\mathbf{N}_{ij})$ first and then to recover the full joint PDF $p(\boldsymbol{X})$ through a sequential probability sampling.

2.2 Data template and multiple-point statistics

Statistical characteristic of pixel patterns within the local region $LR(X_{ij}, \mathbf{N}_{ij})$ is also called multiple-point statistics (MPS) in literature (Okabe and Blunt, 2005; Hajizadeh et al., 2011; Wu et al., 2018). The shape and size of the local region are important to the associated MPS, and different data templates have been designed for MPS calculation, as shown in Figure 2. Data template is used to collect primary local patterns from the digital image $\boldsymbol{X}$, and then the associated MPS, such as the local PDF $p(X_{ij}, \mathbf{N}_{ij})$, can be derived from the occurrence frequencies of data events $(X_{ij}, \mathbf{N}_{ij})$.

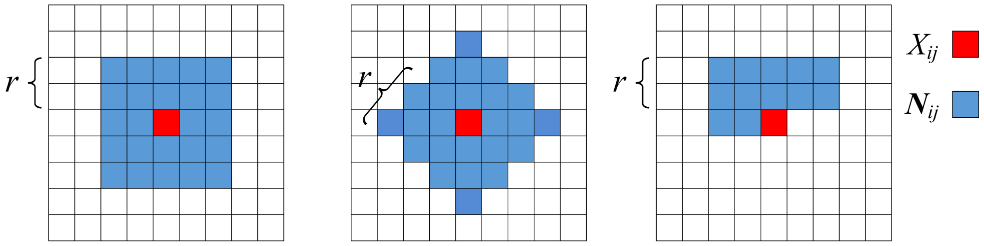

(a) (b) (c)

Figure 2: Different data templates used to model the multiple-point statistics: (a) Square-shaped, (b) Diamond-shaped, and (c) L-shaped data template (the size of a data template is measured by its radius r).

In this work, the L-shaped data template (as shown in Figure 2c) is adopted, because the neighbouring pixels $\mathbf{N}_{ij}$ are all prior to the central pixel X_{ij} in the raster scan order. This feature is very important to the proposed microstructure reconstruction method, and more detailed explanation will be provided in § 3. The data template is used to scan the training image $\boldsymbol{X}$ in the raster scan order, to collect data events $(X_{ij}, \mathbf{N}_{ij})$, as illustrated in Figure 3. The configuration of a data event $(X_{ij}, \mathbf{N}_{ij})$ usually varies with the pixel location (i, j), and each data event represents a variation of local spatial pattern in the training image. The collection of data events starts from the top left pixel that has enough neighbouring pixels to fit the data template. As to the pixels on the borders, they will not be scanned as central pixels due to the absence of some neighbourhoods.

The MPS associated with the data template can be approximated as the occurrence frequencies of the data events collected from the training image, given by:

$$p(X_{ij}, \mathbf{N}_{ij}) = \frac{O(X_{ij}, \mathbf{N}_{ij})}{\sum O(X_{ij}, \mathbf{N}_{ij})} = \frac{O(X_{ij}, \mathbf{N}_{ij})}{O_{\text{all}}} \tag{3}$$

$$p(\mathbf{N}_{ij}) = \frac{O(\mathbf{N}_{ij})}{\sum O(\mathbf{N}_{ij})} = \frac{O(\mathbf{N}_{ij})}{O_{\text{all}}} \tag{4}$$

where $O(X_{ij}, \mathbf{N}_{ij})$ and $O(\mathbf{N}_{ij})$ are the occurrence times of data events $(X_{ij}, \mathbf{N}_{ij})$ and $(\mathbf{N}_{ij})$ respectively, and O_{all} is the total number of data events.

For statistical characterization of microstructural complexity, the core issue here is to determine the local CPDF $p(X_{ij}|\mathbf{N}_{ij})$, which provides the probability of a pixel's phase value given the phase values of its neighbours. Mathematically, the local CPDF $p(X_{ij}|\mathbf{N}_{ij})$ can be calculated from the local PDFs $p(X_{ij}, \mathbf{N}_{ij})$ and $p(\mathbf{N}_{ij})$, given by:

$$p(X_{ij}|\mathbf{N}_{ij}) = \frac{p(X_{ij}, \mathbf{N}_{ij})}{p(\mathbf{N}_{ij})} = \frac{O(X_{ij}, \mathbf{N}_{ij})}{O(\mathbf{N}_{ij})} \tag{5}$$

2.3 Implicit modelling of CPDF via supervised machine learning

Explicit modelling of the local CPDF $p(X_{ij}|\mathbf{N}_{ij})$ is often computationally intractable, especially for heterogeneous media with extremely complicated microstructures. In this study, the local CPDF $p(X_{ij}|\mathbf{N}_{ij})$ is implicitly constructed by using the data events $(X_{ij}, \mathbf{N}_{ij})$ collected from the training image $\boldsymbol{X}$ to fit a supervised machine learning model. The properly fitted machine learning model can be consider as an implicit representation of $p(X_{ij}|\mathbf{N}_{ij})$, from which the full joint PDF $p(\mathbf{X})$ can be recovered through a sequential probability sampling. The main procedure to statistically characterize 2D cross-sectional images via supervised machine learning is summarized in Algorithm 1.

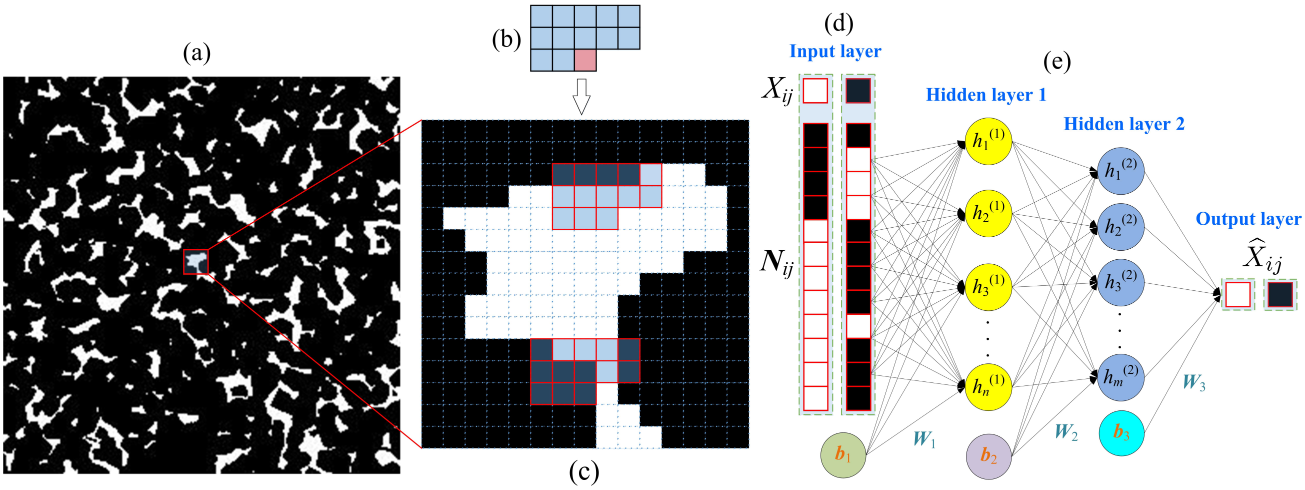

Figure 3: Graphical illustration of the implicit modelling process of the CPDF $p(X_{ij}|\mathbf{N}_{ij})$ via supervised machine learning: (a) A representative 2D slice is selected as the 2D training image $\boldsymbol{X}$; (b) The L-shaped data template is used to collect data events from the training image (the radius r should be set large enough to cover the primary morphological features of the training image, and more details can be found in § 3.3); (c) Pixel grid can be seen in the partial zoom of the training image, and two examples of data events $(X_{ij}, \mathbf{N}_{ij})$ are given; (d) The set of neighboring pixels $\mathbf{N}_{ij}$ are reshaped to be a feature vector, and corresponding central pixel X_{ij} is used as the label category for training the machine learning model; and (e) Based on the collected data events, a shallow neural network model with 2 hidden layers is fitted to implicitly represent the CPDF $p(X_{ij}|\mathbf{N}_{ij})$.

For a digital microstructure with two distinct phases, the phase value of each pixel can only be 1 (white) or 0 (black). Therefore, the CPDF $p(X_{ij}|\mathbf{N}_{ij})$ can be equivalent to the class probability in a binary classification

Algorithm 1: Statistical characterization of 2D cross-sectional images via supervised machine learning

```
Data: The 2D training image $\boldsymbol{X}$ of size $l \times w$;
Data: The 2D data template with neighbouring radius equal to $r$.
for $r+1 \leq i \leq l$ do
    for $r+1 \leq j \leq w-r$ do
        Collect data events $(X_{ij}, \mathbf{N}_{ij})$ from the traing image $\boldsymbol{X}$ by using the selected 2D data template;
        Rearrange the neighbouring data $\mathbf{N}_{ij}$ into a feature vector;
        Move the 2D data template to the next postion follwing the raster scan order: $j = j+1$;
    end
    Move the 2D data template to the next line: $i = i+1$.
end
Model training: Train an ANN model $\boldsymbol{M}$ by using the collected data events $(X_{ij}, \mathbf{N}_{ij})$.
Return: The fitted ANN model $\boldsymbol{M}$ (the implicit representation of CPDF $p(X_{ij}|\mathbf{N}_{ij})$).
```

problem, where X_{ij} is the classification category and $\mathbf{N}_{ij}$ is the classification features. The data events $(X_{ij}, \mathbf{N}_{ij})$ collected from the training image are paired observations, and they are perfect training data to fit a supervised machine learning model for classification purpose, as illustrated in Figure 3. Fed by data events $(X_{ij}, \mathbf{N}_{ij})$, the classifier can be built by minimize the probability of misclassification for any input features $\mathbf{N}_{ij}$, and the class probability (Murphy, 2012) stored in the properly trained machine learning model will be an accurate estimation of the CPDF $p(X_{ij}|\mathbf{N}_{ij})$.

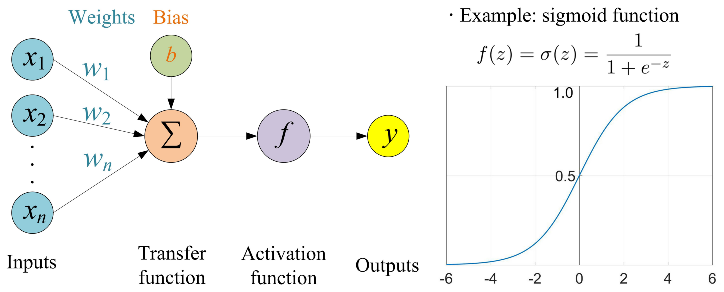

Figure 4: Graphic illustration of a basic neuron.

Commonly-used supervised learning algorithms (Kotsiantis et al., 2007), including decision tree, artificial neural networks (ANN) and support vector machine, are all able to fulfill this classification task. In this study, the ANN model with a shallow architecture is found particularly suitable to capture the microstructural complexities, because it possesses a powerful capacity in analysing complex data and exploring hidden rules associated with random microstructures. ANN can be considered as function approximations to map inputs to outputs through many interconnected computation elements called neurons (Yegnanarayana, 2009). Each elementary neuron possesses a certain degree of approximation capacity, and a powerful learning performance can be achieved by cohesively combining many neurons. In a basic neuron, as illustrated in Figure 4, the weighted sum of inputs x_i plus the bias b is calculated through a transfer function, and the sum is then fed to a non-linear activation function to obtain an output y:

$$y = f\left(\sum_{k=1}^{n} w_k x_k + b\right) \tag{6}$$

where n is the number of inputs, w_k denotes the weight, and f denotes the activation function, which can be a sigmoid function, hyperbolic tangent function or rectified linear unit. Many basic neurons can be connected in various ways to form a multilayer architecture, called neural networks, where the output from a prior neuron is used as the input of the following neuron.

In this study, the hyperbolic tangent function $\tanh(z)$ is adopted as the activation function for hidden layers, which transforms the continuous data z into a value between -1 and 1:

$$\tanh(z) = \frac{e^{z} - e^{-z}}{e^{z} + e^{-z}} \tag{7}$$

The sigmoid function $\sigma(z)$ is connected with the output layer, which transforms the continuous data z into a probability between 0 and 1:

$$\sigma(z) = \frac{1}{1 + e^{-z}} \tag{8}$$

When using the data events $(X_{ij}, \boldsymbol{N}_{ij})$ to train an ANN model, the neighbouring pixels $\boldsymbol{N}_{ij}$ play the role as input feature, and the central pixel X_{ij} is the label data (classification category), as illustrated in Figure 3. It is noted that the format of $\boldsymbol{N}_{ij}$ is rearranged into an array before inputting them to the ANN model, as illustrated in Figure 3d. The final output $\widehat{X}_{ij}$ is computed through a series of forward-propagation equations that occur at particular layers, given by:

$$\boldsymbol{H}^{(0)} = \boldsymbol{N}_{ij} \tag{9}$$

$$\boldsymbol{H}^{(1)} = \tanh\left(\boldsymbol{W}_1^{\mathrm{T}} \boldsymbol{N}_{ij} + b_1\right) \tag{10}$$

$$\boldsymbol{H}^{(2)} = \tanh\left(\boldsymbol{W}_2^{\mathrm{T}} \boldsymbol{H}^{(1)} + b_2\right) \tag{11}$$

$$\widehat{X}_{ij} = \sigma\left(\boldsymbol{W}_3^{\mathrm{T}} \boldsymbol{H}^{(2)} + b_3\right) \tag{12}$$

where $\boldsymbol{H}^{(k)}$ denotes the output of the k-th hidden layer, $\boldsymbol{W}_k$ is the weight matrix and b_k is the bias vector.

The training procedure is to minimize the errors between observations X_{ij} and predictions $\widehat{X}_{ij}$ by adjusting the weight matrices $\boldsymbol{W}$ and bias vectors $\boldsymbol{b}$. This discrepancy is represented by a loss function $\mathcal{L}(\boldsymbol{W}, \boldsymbol{b})$ as follows:

$$\underset{\boldsymbol{W}, \boldsymbol{b}}{\arg\min} \;\; \mathcal{L}(\boldsymbol{W}, \boldsymbol{b}) = \frac{1}{m} \sum \left\| \widehat{X} - X \right\|_2^2 \tag{13}$$

where m is the number of data events used to train the ANN model.

Stochastic optimization algorithms are usually used to solve the above minimization problem (Kotsiantis et al., 2007; Yegnanarayana, 2009). Considering the shallow architectures of the ANN models used in this study, we adopt the scaled conjugate gradient (SCG) method to obtain the optimal weights and bias. As summarized in Algorithm 2, SCG optimizer is iteratively performed for a sufficient number of epochs to obtained a converged neural networks, and more details about it can be found in Møller (1993). Besides, cross-validation is usually performed to avoid overfitting, thereby to improve the generalized predictive ability for new observations. More details about stochastic optimization and cross-validation of neural networks can be found in Kotsiantis et al. (2007) and Yegnanarayana (2009).

After the ANN model is properly trained, this model is able to predict the response for a new observation $\boldsymbol{N}_{\text{new}}$. Because the final prediction $\widehat{X}_{\text{new}}$ is output from a sigmoid function, its value is between 0 and 1 for the binary training image. $\widehat{X}_{\text{new}}$ is equal to the class probability corresponding to the input feature, which is also an accurate approximation to the CPDF $p(X_{ij}|\boldsymbol{N}_{ij})$ in Eq. (5). Therefore, the fitted ANN model can be considered as an implicit representation of the CPDF $p(X_{ij}|\boldsymbol{N}_{ij})$ that statistically characterizes the 2D training image $\boldsymbol{X}$. Considering the easy access to various open-source toolboxes of supervised learning, the proposed method can be quickly implemented for the purpose of statistical microstructure characterization. It should be noted that this machine learning-based characterization method can also be used for multi-phase media, although only bi-phase microstructures are introduced in this section.

3 Stochastic reconstruction of 3D microstructures

Generally, a 2D cross-sectional image cannot completely represent the corresponding 3D microstructure that contains a stack of 2D slices, but it possesses similar statistical characteristics as the 3D one and can be considered as a random realization of 3D morphology projecting onto a 2D plane (Wu et al., 2006). If the 3D microstructure is stationary, a 2D slice of proper size can be used as an effective representative for all layers in the same direction (Tahmasebi and Sahimi, 2012). In such cases, it is possible and feasible to infer statistically and morphologically realistic 3D microstructures from the 2D reference images.

Algorithm 2: The scaled conjugate gradient (SCG) algorithm for training artificial neural networks

```
Data: Data events $(X, \boldsymbol{N})$ for ANN model training;
Data: Epoch number $K_{\mathrm{epo}}$.
Initialize the parameters: $\boldsymbol{W}, \boldsymbol{b} \leftarrow \mathrm{Init}(\boldsymbol{W}, \boldsymbol{b})$;
for $k \leq K_{\mathrm{epo}}$ do
    Compute the ANN model output: $\widehat{X} \leftarrow ANN(\boldsymbol{W}, \boldsymbol{b}, \boldsymbol{N})$;
    Compute the loss function: $\mathcal{L}(\boldsymbol{W}, \boldsymbol{b}) \leftarrow \frac{1}{m} \sum \left\| \widehat{X} - X \right\|_2^2$;
    Compute the gradients: $\frac{\partial \mathcal{L}}{\partial \boldsymbol{W}}$ and $\frac{\partial \mathcal{L}}{\partial \boldsymbol{b}}$;
    Determine the steepest descent direction $p_k$ and the step size $\alpha_k$ according to the gradients:
    $p_k \leftarrow \mathcal{F}_{\mathrm{scg}}(\frac{\partial \mathcal{L}}{\partial \boldsymbol{W}}, \frac{\partial \mathcal{L}}{\partial \boldsymbol{b}})$, $\alpha_k \leftarrow \mathcal{G}_{\mathrm{scg}}(\frac{\partial \mathcal{L}}{\partial \boldsymbol{W}}, \frac{\partial \mathcal{L}}{\partial \boldsymbol{b}})$; % Note: $\mathcal{F}_{\mathrm{scg}}$ and $\mathcal{G}_{\mathrm{scg}}$ are the computing operations in the SCG
      method, and more details can be found in the relevent reference.
    Updata the parameters: $\boldsymbol{W} \leftarrow \boldsymbol{W} + \alpha_k p_k$, $\boldsymbol{b} \leftarrow \boldsymbol{b} + \alpha_k p_k$.
end
$\boldsymbol{W}_{\mathrm{optimal}} \leftarrow \boldsymbol{W}$, $\boldsymbol{b}_{\mathrm{optimal}} \leftarrow \boldsymbol{b}$.
Return: $\boldsymbol{W}_{\mathrm{optimal}}$ and $\boldsymbol{b}_{\mathrm{optimal}}$.
```

3.1 Morphology integration

In § 2, the statistical characteristics (i.e. the CPDF $p(X_{ij}|\boldsymbol{N}_{ij})$) of the 2D cross-sectional image have been implicitly modelled in a supervised learning paradigm, and the next key issue is how to generate statistically equivalent 3D microstructure samples based on this 2D characterization. As introduced in § 1, the supervised learning-based method (SLM) (Bostanabad et al., 2016a,b) has already been used for equidimensional reconstruction of heterogeneous microstructures. Its reconstruction process can be interpreted as a stochastic recombination of local morphology patterns that are learned by the fitted supervised learning model, where only the size expansion occurs during the reconstruction process. While for the 2D-to-3D microstructure reconstruction, both size expansion and dimension upgrade of local morphology patterns are involved. Therefore, an information integration scheme is required to project the 2D morphological statistics into the 3D space, thereby achieving the objective of 2D-to-3D microstructure reconstruction.

As explained in § 2, the MRF assumption associated with the L-shaped data template is adopted for statistical characterization of 2D training images. For 3D microstructure characterization and reconstruction, the MRF assumption is still applicable, and it states that the phase value of a voxel Y_{ijk} at any site of the 3D image only depends on its neighbours $\boldsymbol{N}_{ijk}$ within a large enough region. Here, we further simplify the MRF assumption, where the value of a voxel only depends on its neighbouring voxels on three orthogonal planes: xy-, yz- and zx-planes within a sufficiently large range. For isotropic 3D microstructures, the morphological statistics on three orthogonal planes can be considered to be identical, which means the machine learning model that statistically characterizes the 2D slices on xy-plane can also be used for that on yz- and zx-planes. While for anisotropic 3D microstructures, different machine learning models should be trained separately to statistically characterize the 2D slices on three orthogonal planes, so as to capture the anisotropic property.

The key issue to address is how to integrate the 2D morphological statistics on three separate planes into the morphological statistics in 3D space. To bridge the gap between 2D characterization and 3D reconstruction, a special 3D data template is thus created by combining three 2D L-shaped data templates on orthogonal planes, as graphically illustrated in Figure 5. We establish the relationship between the 3D CPDF ($p(Y_{ijk}|\boldsymbol{N}_{ijk})$) and the 2D CPDFs ($p\left(Y_{ijk}\middle|\boldsymbol{N}_{ijk}^{(xy)}\right)$, $p\left(Y_{ijk}\middle|\boldsymbol{N}_{ijk}^{(yz)}\right)$ and $p\left(Y_{ijk}\middle|\boldsymbol{N}_{ijk}^{(zx)}\right)$) through weighted average, given by:

$$
\begin{aligned}
p\left(Y_{ijk}|\boldsymbol{N}_{ijk}\right) &= p\left(Y_{ijk}\middle|\boldsymbol{N}_{ijk}^{(zx)}, \boldsymbol{N}_{ijk}^{(xy)}, \boldsymbol{N}_{ijk}^{(yz)}\right) \\
&\approx \frac{1}{3} \cdot \left[p\left(Y_{ijk}\middle|\boldsymbol{N}_{ijk}^{(xy)}\right) + p\left(Y_{ijk}\middle|\boldsymbol{N}_{ijk}^{(yz)}\right) + p\left(Y_{ijk}\middle|\boldsymbol{N}_{ijk}^{(zx)}\right) \right]
\end{aligned}
\tag{14}
$$

where $\boldsymbol{N}_{ijk}^{(xy)}$, $\boldsymbol{N}_{ijk}^{(yz)}$ and $\boldsymbol{N}_{ijk}^{(zx)}$ are the neighbouring voxels on xy-, yz- and zx-planes, respectively.

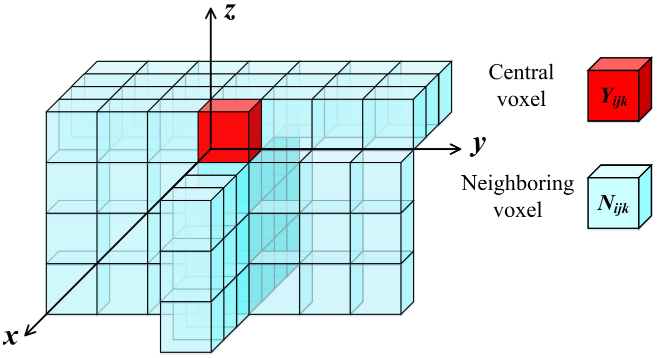

Figure 5: A 3D data template composed by three 2D L-shaped data templates on orthogonal planes.

The properly pretrained ANN model is an implicit representation of the 2D CPDF with high accuracy, therefore, the 3D CPDF $p(Y_{ijk}|\mathbf{N}_{ijk})$ can be calculated as follows:

$$p\left(Y_{ijk}|\mathbf{N}_{ijk}\right) \approx \frac{1}{3} \cdot \left(p_{ijk}^{(xy)} + p_{ijk}^{(yz)} + p_{ijk}^{(zx)}\right) \tag{15}$$

where $p_{ijk}^{(xy)}$, $p_{ijk}^{(yz)}$ and $p_{ijk}^{(zx)}$ are the class probability values stored in the fitted ANN models. For 3D isotropic reconstruction, $p_{ijk}^{(xy)}$, $p_{ijk}^{(yz)}$ and $p_{ijk}^{(zx)}$ can be extracted from the same ANN model. For 3D anisotropic reconstruction, $p_{ijk}^{(xy)}$, $p_{ijk}^{(yz)}$ and $p_{ijk}^{(zx)}$ should be extracted from three different ANN models that are separately trained by using the data events collected from xy-, yz- and zx-planes, respectively.

3.2 Microstructure reconstruction procedure

In the above section, the 3D CPDF $p(Y_{ijk}|\mathbf{N}_{ijk})$ has been inferred from three 2D CPDFs $p\left(Y_{ijk}\middle|\mathbf{N}_{ijk}^{(xy)}\right)$, $p\left(Y_{ijk}\middle|\mathbf{N}_{ijk}^{(yz)}\right)$ and $p\left(Y_{ijk}\middle|\mathbf{N}_{ijk}^{(zx)}\right)$ through the morphology integration scheme, and it can be used to produce statistically equivalent 3D microstructures via a procedure of sequential probability sampling. Suppose there is an underlying full joint PDF $p(\mathbf{Y})$ of the 3D reconstructed sample $\mathbf{Y}$, and it can be expressed in a factorial from as follows:

$$\begin{aligned} p(\mathbf{Y}) &= p(Y_{111})p(Y_{112}|Y_{111})p(Y_{113}|Y_{111},Y_{112})\cdots p\left(Y_{ijk}|Y_{111},Y_{112},Y_{113}\cdots Y_{ij(k-1)}\right)\cdots \\ &= p(Y_{111})\,p\left(Y_{112}\middle|\mathbf{Y}^{(<112)}\right)p\left(Y_{113}\middle|\mathbf{Y}^{(<113)}\right)\cdots p\left(Y_{ijk}\middle|\mathbf{Y}^{(<ijk)}\right)\cdots \end{aligned} \tag{16}$$

where $\mathbf{Y}^{(<ijk)}$ represents the voxel sequence ahead of the voxel Y_{ijk}.

If all factors $p\left(Y_{ijk}\middle|\mathbf{Y}^{(<ijk)}\right)$ in Eq. (16) are known, it is feasible to sequentially generate voxels by probability sampling from $p\left(Y_{ijk}\middle|\mathbf{Y}^{(<ijk)}\right)$, and the generated voxel sequence is a random realization of the full joint PDF $p(\mathbf{Y})$. To be specific, the voxel Y_{111} is firstly generated from $p\left(Y_{111}\middle|\mathbf{Y}^{(<111)}\right)$ with a random initialization of $\mathbf{Y}^{(<111)}$, and then the voxel Y_{112} is generated from $p\left(Y_{112}\middle|\mathbf{Y}^{(<112)}\right)$ conditional to Y_{111}. The remaining voxels can all be generated through the same procedure. When the voxel sequence is sufficiently long, the effect of initialization can be ignored.

As illustrated in Figure 5, the neighbouring voxels $\mathbf{N}_{ijk}$ in the 3D data template are all in front of the central voxels Y_{ijk} in the raster scan order, so $\mathbf{N}_{ijk}$ is contained in $\mathbf{Y}^{(<ijk)}$ (mathematically, it is expressed as $\mathbf{N}_{ijk} \subset \mathbf{Y}^{(<ijk)}$). In view of the MRF assumption, the following relationship holds:

$$p\left(Y_{ijk}\middle|\mathbf{Y}^{(<ijk)}\right) = p(Y_{ijk}|\mathbf{N}_{ijk}) \tag{17}$$

Substituting Eq. (17) into Eq. (16), the full joint PDF $p(\boldsymbol{Y})$ is rewritten as the following form:

$$p(\boldsymbol{Y}) = p(Y_{111})p(Y_{112}|\mathbf{N}_{112})p(Y_{113}|\mathbf{N}_{113})\cdots p(Y_{ijk}|\mathbf{N}_{ijk})\cdots \tag{18}$$

where each factor $p(Y_{ijk}|\mathbf{N}_{ijk})$ can be estimated from Eq. (15). The class probabilities in Eq. (15) can be directly extracted from the fitted ANN models by inputting the neighbouring voxels. After all voxels Y_{ijk} are generated from the sequential probability sampling, a new 3D microstructure $\boldsymbol{Y}$ is completely reconstructed, and it is statistically equivalent to the 2D training images $\boldsymbol{X}$.

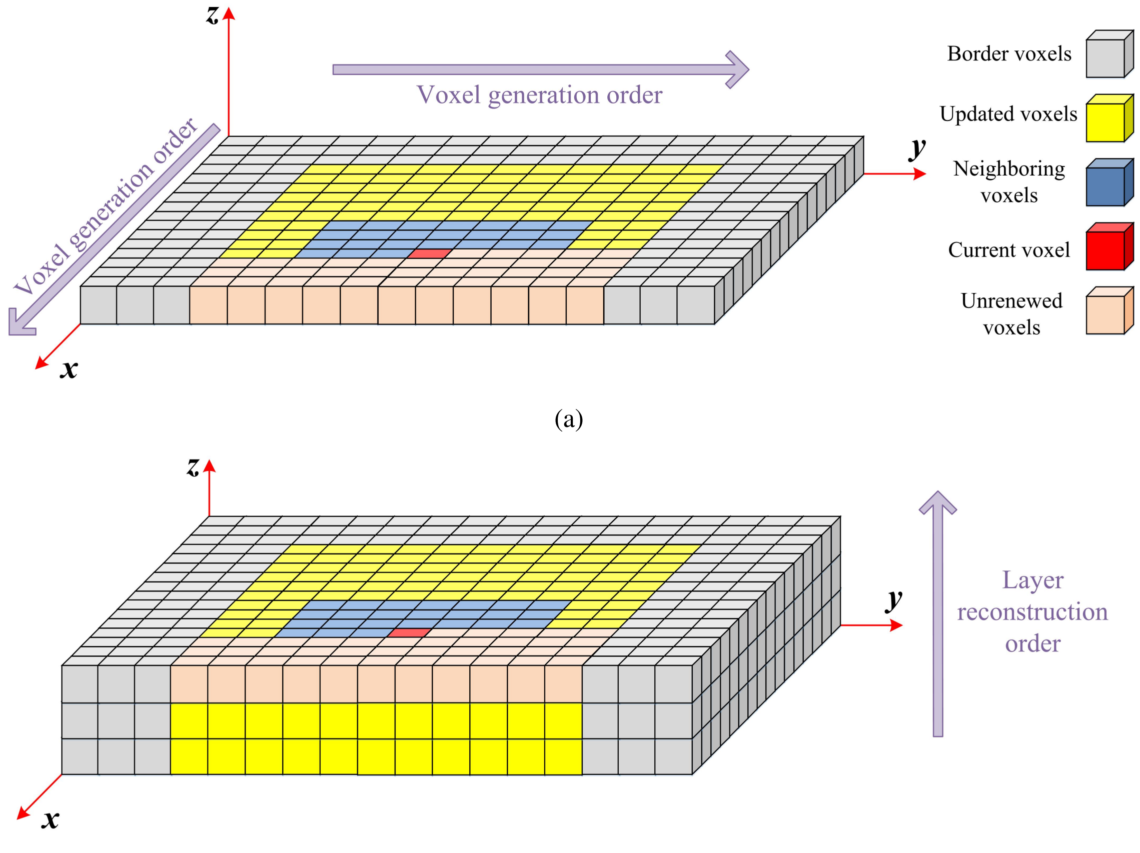

(a)

(b)

Figure 6: Graphical illustration of the 3D microstructure reconstruction procedure: (a) Reconstruction of the 1st layer; and (b) Reconstruction of the 3rd layer.

The main procedure of the developed 2D-to-3D reconstruction method is summarized in Algorithm 3. Starting from an initial guess $\boldsymbol{Y}_0$, the 3D microstructure sample $\boldsymbol{Y}$ is reconstructed through a layer-by-layer procedure, and voxels on each layer are generated one by one in the raster scan order, as illustrated in Figure 6. The phase value of each voxel Y_{ijk} is assigned by probability sampling from the CPDF $p(Y_{ijk}|\mathbf{N}_{ijk})$. This CPDF $p(Y_{ijk}|\mathbf{N}_{ijk})$ is calculated from Eq. (15), where the class probabilities $p_{ijk}^{(xy)}$, $p_{ijk}^{(yz)}$ and $p_{ijk}^{(zx)}$ are obtained by inputting the neighbouring voxels $\mathbf{N}_{ijk}^{(xy)}$, $\mathbf{N}_{ijk}^{(yz)}$ and $\mathbf{N}_{ijk}^{(zx)}$ into the pretrained supervised machine learning models $\boldsymbol{M}^{(xy)}$, $\boldsymbol{M}^{(yz)}$, and $\boldsymbol{M}^{(zx)}$, respectively.

In the construction of the first few layers, the neighbourhood ranges on yz- and zx-planes are smaller than the predefined radii r_{yz} and r_{zx} respectively, and these few layers are called the transition zone. For instance, there is no voxel in $\mathbf{N}_{ij1}^{(yz)}$ and $\mathbf{N}_{ij1}^{(zx)}$ for the reconstruction of the 1st layer, which means only the neighbouring voxels $\mathbf{N}_{ij1}^{(xy)}$ on xy-plane (with neighbouring radius equal to r_{xy}) is needed to construct the 1st layer. In the construction of this transition zone, the neighbouring radii of $\mathbf{N}_{ijk}^{(yz)}$ and $\mathbf{N}_{ijk}^{(zx)}$ gradually increase, as more layers are generated. As can be seen in Figure 7, the radii $\mathbf{N}_{ijk}^{(xy)}$, $\mathbf{N}_{ijk}^{(yz)}$ and $\mathbf{N}_{ijk}^{(zx)}$ are equal to r_{xy}, 2 and 2 voxels

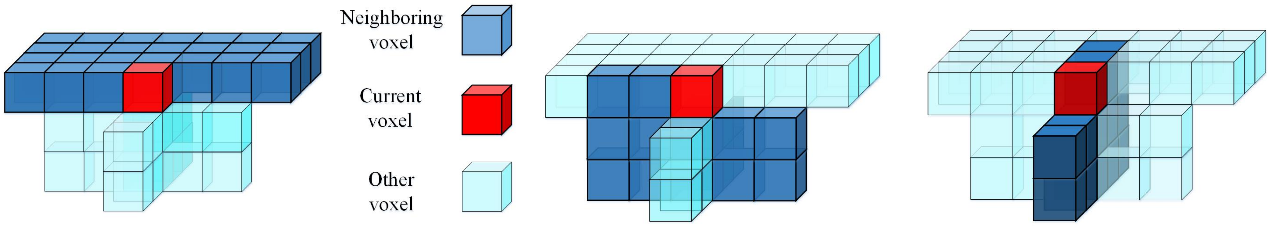

(a) (b) (c)

Figure 7: Decompose of a 3D data template: (a) Neighbourhood area on xy-plane with $r_{xy} = 3$ voxels; (b) Neighbouring area on yz-plane with $r_{yz} = 2$ voxels; and (c) Neighbourhood area on zx-plane with $r_{zx} = 2$ voxels.

respectively, for the reconstruction of the 3rd layer. Therefore, multiple ANN models are required to meet the variations of neighbouring ranges on yz- and zx-planes. As layer construction enters the steady zone, the sizes of $\mathbf{N}_{ijk}^{(yz)}$ and $\mathbf{N}_{ijk}^{(zx)}$ are fixed to be the predefined values r_{yz} and r_{zx} respectively, where the same ANN models capturing the basic morphology features are used repeatedly. To ensure microstructure reconstruction quality, only the steady zone will be kept as the final result of reconstructed sample.

3.3 Data template size and boundary setting

The radii r of the 2D and 3D data templates are important parameters for both microstructure characterization and reconstruction, and need to be properly determined. Generally, the size of a data template should be large enough to cover the primary features of training images. The effect of data template size on microstructure reconstruction has been systematically investigated in Fu et al. (2021a). Here, we only briefly introduce the determination method of the data template size for a specific training image.

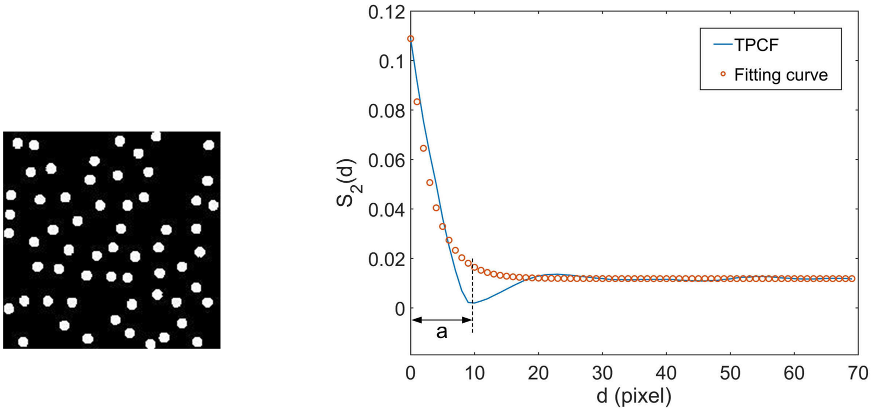

(a) (b)

Figure 8: (a) A 2D training image; (b) Two-point correlation function (TPCF) and its fitting curve (Fu et al., 2021a).

The 2D training image of an isotropic microstructure is given in Figure 8a, based on which the influence of data template size on microstructure reconstruction is investigated. Figure 9 shows the reconstruction results by using data templates with different radii r. It is clear that the reconstruction quality becomes better as the data template size increases, until r reaches a critical value. This critical value is the minimum value of r to cover the primary morphological features of the training image. The correlation length a is found to be a good approximation of the critical radius r_c, and it can be directly measured from the two-point correlation function (TPCF) curve, as illustrated in Figure 8b. Besides, the correlation length a can also be computed by fitting the

Algorithm 3: Stochastic reconstruction of 3D microstructures using the machine learning-based characterization of 2D cross-sectional images

```
Data: The pretrained machine learning models $\boldsymbol{M}$;
Data: The predefined values of neighbouring radii $r_{xy}$, $r_{yz}$ and $r_{zx}$ for the 3D data template;
Initialization: Assign binary white noise to the 3D lattice grid of size $I \times J \times K$ as the initial guess $\mathbf{Y}_0$.
Construction of the transition zone: $r = \max(r_{yz}, r_{zx})$
for $k \leq r$ do
    Select the pretrained supervised machine learning models $\boldsymbol{M}^{(xy)}_{(r_{xy})}$, $\boldsymbol{M}^{(yz)}$, and $\boldsymbol{M}^{(zx)}$;
    Select the 3D data templates of suitable sizes;
    for $r+1 \leq i \leq I$ and $r+1 \leq j \leq J-r$ do
        Use the 3D data template to collect the neighbouring voxels $\boldsymbol{N}_{ijk}$ from $\mathbf{Y}_0$, including $\boldsymbol{N}^{(xy)}_{ijk}$, $\boldsymbol{N}^{(yz)}_{ijk}$ and $\boldsymbol{N}^{(zx)}_{ijk}$ on three orthogonal planes;
        Rearrange the neighbouring data $\boldsymbol{N}^{(xy)}_{ijk}$, $\boldsymbol{N}^{(yz)}_{ijk}$ and $\boldsymbol{N}^{(zx)}_{ijk}$ into arrays;
        Extract class probabilities $p^{(xy)}_{ijk}$, $p^{(yz)}_{ijk}$ and $p^{(zx)}_{ijk}$ from the pretrained machine learning models $\boldsymbol{M}^{(xy)}_{(r_{xy})}$, $\boldsymbol{M}^{(yz)}$, and $\boldsymbol{M}^{(zx)}$ by inputing $\boldsymbol{N}^{(xy)}_{ijk}$, $\boldsymbol{N}^{(yz)}_{ijk}$ and $\boldsymbol{N}^{(zx)}_{ijk}$ repectively;
        Compute the CPDF $p(Y_{ijk}|\boldsymbol{N}_{ijk})$ according to Eq. (15);
        Generate a phase value through probability sampling from the CPDF $p(Y_{ijk}|\boldsymbol{N}_{ijk})$, and use it to update the phase value of current voxel $Y_{ijk}$;
        Move the 3D data template to next voxel following the raster scan order;
    end
    Set periodic/reflective boudary to the $k$-th layer, and repeat the above procedure for 1 or 2 time(s);
    Denoise and smooth the newly constructed layer $k$, and move to the next layer: $k = k+1$;
    Increase the neighbouring radii of $\boldsymbol{N}^{(yz)}_{ijk}$ and $\boldsymbol{N}^{(zx)}_{ijk}$ by 1, until meeting the predefined $r_{yz}$ and $r_{zx}$.
end
Construction of the steady zone:
for $r+1 \leq k \leq K$ do
    Select the pretrained supervised machine learning models $\boldsymbol{M}^{(xy)}_{(r_{xy})}$, $\boldsymbol{M}^{(yz)}_{(r_{yz})}$, and $\boldsymbol{M}^{(zx)}_{(r_{zx})}$;
    Select the 3D data template with the neighbouring radii on $xy$-, $yz$- and $zx$-plane equal to $r_{xy}$, $r_{yz}$ and $r_{zx}$ respectively;
    for $r+1 \leq i \leq I$ and $r+1 \leq j \leq J-r$ do
        Use the 3D data template to collect the neighbouring voxels $\boldsymbol{N}_{ijk}$ from $\mathbf{Y}_0$, including $\boldsymbol{N}^{(xy)}_{ijk}$, $\boldsymbol{N}^{(yz)}_{ijk}$ and $\boldsymbol{N}^{(zx)}_{ijk}$ on three orthogonal planes;
        Rearrange the neighbouring data $\boldsymbol{N}^{(xy)}_{ijk}$, $\boldsymbol{N}^{(yz)}_{ijk}$ and $\boldsymbol{N}^{(zx)}_{ijk}$ into arrays;
        Extract class probabilities $p^{(xy)}_{ijk}$, $p^{(yz)}_{ijk}$ and $p^{(zx)}_{ijk}$ from the pretrained machine learning models $\boldsymbol{M}^{(xy)}_{(r_{xy})}$, $\boldsymbol{M}^{(yz)}_{(r_{yz})}$, and $\boldsymbol{M}^{(zx)}_{(r_{zx})}$ by inputing $\boldsymbol{N}^{(xy)}_{ijk}$, $\boldsymbol{N}^{(yz)}_{ijk}$ and $\boldsymbol{N}^{(zx)}_{ijk}$ respectively;
        Compute the CPDF $p(Y_{ijk}|\boldsymbol{N}_{ijk})$ according to Eq. (15);
        Generate a phase value through probability sampling from the CPDF $p(Y_{ijk}|\boldsymbol{N}_{ijk})$, and use it to update the phase value of current voxel $Y_{ijk}$;
        Move the 3D data template to next voxel following the raster scan order;
    end
    Set periodic/reflective boudary to the $k$-th layer, and repeat the above procedure for 1 or 2 time(s);
    Denoise and smooth the newly constructed layer $k$, and move to the next layer: $k = k+1$;
end
Process the raw 3D reconstruction result.
Return: A 3D statistically equivalent microstructure sample $\boldsymbol{Y}$.
```

TPCF with an exponential function, as defined below (Corson, 1974):

$$S_2(d) = (\phi - \phi^2)\exp(-\frac{3d}{a}) + \phi^2 \tag{19}$$

where $S_2(d)$ denotes TPCF, d denotes the distance between two pixels, and ϕ is the volume fraction of calculated material phase.

For example, the correlation length a of the training image in Figure 8a is calculated to be 9.83 pixels, and the best reconstruction result (Figure 9i) rightly corresponds to r=10 pixels, which confirms the effectiveness of the determination methods. As to the multiphase microstructure, the critical radius r_c can also be determined in the same way, where the largest correlation length should be used as the approximation of r_c.

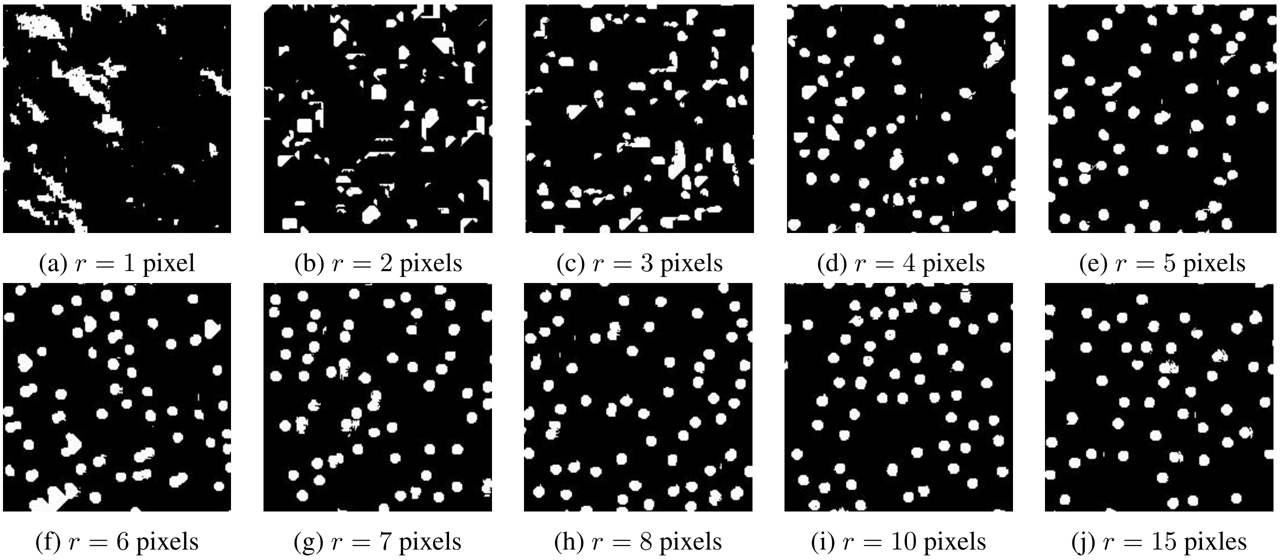
(a) $r = 1$ pixel (b) $r = 2$ pixels (c) $r = 3$ pixels (d) $r = 4$ pixels (e) $r = 5$ pixels

(f) $r = 6$ pixels (g) $r = 7$ pixels (h) $r = 8$ pixels (i) $r = 10$ pixels (j) $r = 15$ pixles

Figure 9: The 2D slices of microstructure reconstruction by using data templates with different radii r (Fu et al., 2021a).

Besides, the boundary setting also has a great influence on the reconstruction quality (Fu et al., 2021a). As illustrated in Figure 6, the border voxels (in gray) on each layer will not be updated, because they do not have enough neighbourhoods as the feature inputs for the pretrained ANN models. However, these boundary voxels still play as neighbourhoods for corresponding inner voxels, and the fixed states of them can bring a negative effect on reconstruction quality, as illustrated in Figure 10a. Fu et al. (2021a) greatly reduced the boundary effect on microstructure reconstruction by setting periodic or reflective boundary condition, as shown in Figure 10b.


(a)

(b)

Figure 10: Boundary effect: (a) The reconstructed slice without setting periodic or reflective boundary; (b) The reconstructed slice with setting reflective boundary (Fu et al., 2021a).

During the reconstruction process of each 2D layer, periodic or reflective boundary condition is adopted here to eliminate the boundary effect. For the first-round reconstruction of a 2D layer, it has borders with random patterns, as shown in Figure 10a. Removing the distorted borders, one can obtain the middle part of the reconstructed layer. Periodic or reflective boundary is then added to this middle part to replace the distorted borders, as illustrated in Figure 11. Treating the newly-obtained 2D slice as the initial guess, one can perform the second-round reconstruction of this layer by following the same reconstruction procedure explained in § 3.2. The boundary effect can be significantly reduced by repeating the above procedures for one or two time(s), and a representative result of the improved outcome is given in Figure 10b.


(a)

(b)

Figure 11: Boundary settings: (a) Periodic boundary condition; (b) Reflective boundary condition.

3.4 Noise reduction and image smoothing

As discussed in previous sections, 2D cross-sectional images cannot completely represent corresponding 3D microstructures, so the real 3D morphology may not be fully inferred and recovered from the 2D supervised learning-based characterization. Due to this incompleteness in microstructure characterization, the statistically reconstructed 3D microstructures are inevitably mingled with noise (Okabe and Blunt, 2005), as illustrated in Figure 12(a) and (b). To enhance the microstructure reconstruction quality, image noise-reduction processing can be performed on the raw reconstruction results. Okabe and Blunt (2005) adopted dilation-erosion processes to smooth the interface of different material components, and additional operation was carried out to adjust the volume fraction of the reconstructed microstructure, through which the 2D-to-3D reconstruction noise is significantly reduced. For porous microstructures, non-percolating solid and pore components may exist in the raw stochastic realizations of 2D-to-3D reconstruction. The non-percolating solid components are isolated islands suspended inside the pore space, which is impossible in the real porous media. Therefore, Liang et al. (1998) directly replaced them by the pore space, and the effect of this replacement had been proved to be negligible. Hajizadeh et al. (2011) directly applied 3D medial filtering to make the raw reconstructed microstructure more visually appealing.

In practice, various image processing measures can be taken to achieve better reconstruction results. Inspired by previous attempts, we enhance the 2D-to-3D reconstruction quality with maintenances of statistical equivalence and morphological similarity through the following steps:

(1) Image processing of the 2D slice after each layer is generated:
  i. Remove the image noise (small isolated particles) through image filtering;
  ii. Perform morphological closing (dilation operation followed by an erosion operation) to improve the connectivity of the secondary phase.
(2) Image process of the 3D microstructure after the entire sample is reconstructed:
  i. Apply 3D image filtering to the raw reconstructed microstructure;
  ii. For porous microstructures, replace the non-percolating solid with the pore space;
  iii. Manually adjust the CPDF $p(Y_{ijk}|\mathbf{N}_{ijk})$ for voxel generation through probability sampling, and repeat the whole reconstruction process if the reference volume fraction is not accurately preserved.

Due to the uncertainties coming from noise reduction and boundary effect, the average volume fraction of reconstruction results can slightly deviate from the reference value. A manual adjustment of the CPDF $p(Y_{ijk}|\mathbf{N}_{ijk})$ is thus required to compensate this deviation:

$$p_{\text{new}}(Y_{ijk}|\mathbf{N}_{ijk}) = \min\Big(\beta p(Y_{ijk}|\mathbf{N}_{ijk}), 1\Big) \tag{20}$$

where β is the adjustment coefficient close to 1. If the average volume fraction of reconstruction results is larger than the reference value, the value of β should be slightly smaller than 1. If it is the other way around, β should have a value slightly larger than 1. There are many factors that can affect the exact value of β, such as initial condition and reconstruction image size. According to our experience, the value of β should fall between 0.995 and 1.005, as recorded in Table 1.

(a) Isotropic microstructure

(b) Anisotropic microstructure

(c) Isotropic microstructure

(d) Anisotropic microstructure

Figure 12: Noise reduction and interface smoothing to improve the 2D-to-3D reconstruction quality: (a) and (b) show the two raw 2D slices before image processing; (c) and (d) show the two enhanced 2D slices after image processing.

3.5 Investigation of rotation effect

Using a machine learning approach, the proposed microstructure reconstruction procedure dose not explicitly process the orientation of reference images. To examine its performance in relation to image rotation, two representative microstructures are considered in this subsection, as shown in Figure 13. The two original images are rotated by 90° clockwise, and all four images are then used as the training images for microstructure reconstruction using the proposed method.

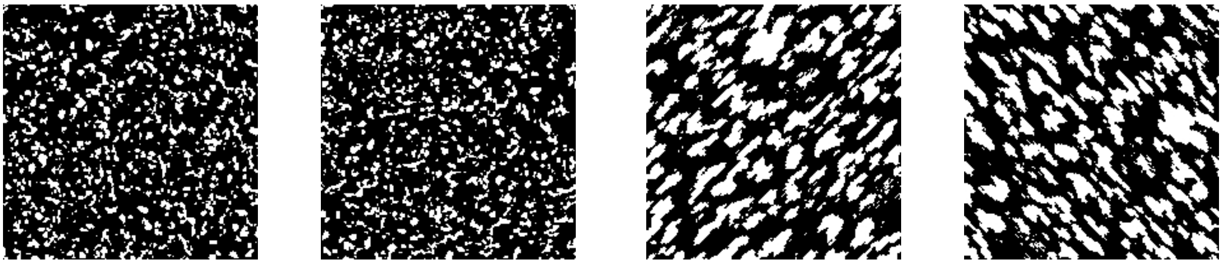

(a) Original

(b) Rotated by 90°

(c) Original

(d) Rotated by 90°

Figure 13: The 2D training images (Bostanabad et al., 2016a): (a) and (b) are the 2D slice of an isotropic microstructure; (c) and (d) are the 2D slice of an anisotropic microstructure.

To simplify this problem, we just statistically reconstructed a group of 2D slices from each training image, and the representative reconstruction results are shown in Figure 14. For the isotropic microstructure shown in Figure 13a and Figure 13b, there is no visible difference between the reconstruction results corresponding to the original and rotated training images. As to the anisotropic microstructure, the reconstruction results are sensitive to the rotation of training images, and they correctly capture such microstructural characteristics as anisotropy and grain orientation distribution.

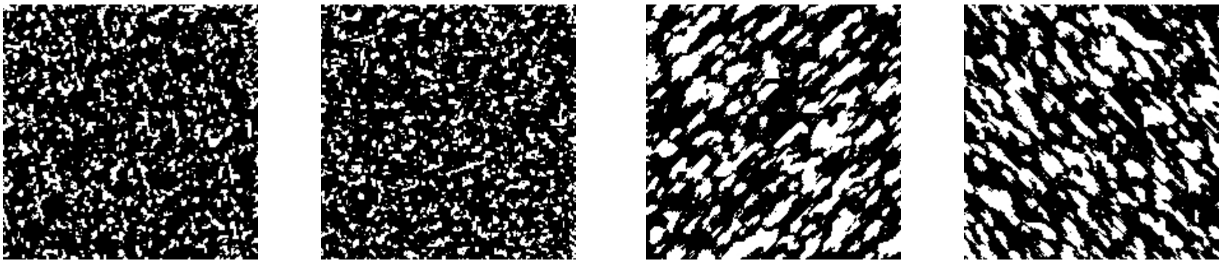

(a) (b) (c) (d)

Figure 14: Reconstructed 2D slices: (a), (b), (c) and (d) are the representative reconstruction results by using the four 2D training images in Figure 13, respectively.

To quantitatively examine the statistical equivalence between the training and reconstructed images, two-point cluster correlation function $C_2(d)$ (see Appendix) and grain orientation distribution $\omega(\theta)$ (see Appendix) are extracted from them for comparison. As shown in Figure 15, the good agreement indicates that the rotation of training images does not bring any negative effect on the preservation of statistical equivalence between the training and reconstructed images. Therefore, from the view of statistical equivalence, the proposed reconstruction method can be considered invariant to training image rotation.

(a) Two-point cluster correlation function (b) Two-point cluster correlation function

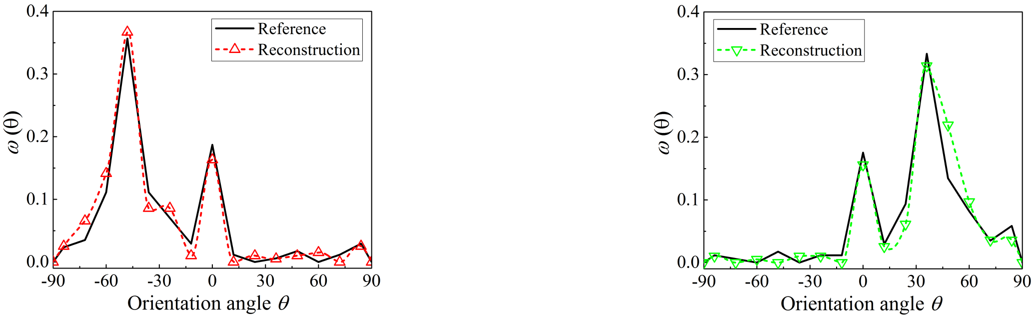

(c) Grain orientation distribution (d) Grain orientation distribution

Figure 15: Statistical comparisons between training images and their reconstruction results: (a), (b), (c) and (d) correspond to the four training images in Figure 13, respectively.

4 Results and comparisons

To test the general applicability of the supervised learning-based method (SLM) in 2D-to-3D microstructure reconstruction, it is applied to a series of heterogeneous microstructures with distinct morphologies. To demonstrate the effectiveness of the proposed method, SLM is also compared with the other two classic reconstruction methods: SOR (Torquato and Yeong, 1998) and GRFT (Liang et al., 1998), in terms of reconstruction accuracy. Basically, reconstruction accuracy (Fu et al., 2021a) indicates how well the inherent stochasticity and microstructural complexities of the original microstructure are preserved by the reconstructed samples.

In each reconstruction case, SOR, GRFT and SLM are used to generate a group of fifty 3D microstructure samples respectively, based on which a comprehensive comparison is conducted. Various types of statistical/morphological descriptors (Torquato, 2002; Hilfer, 2002; Cui et al., 2021), reflecting the statistical equivalence or morphological similarity between the 3D reconstructed and reference microstructures, are adopted here to assess the reconstruction quality. Explanations of these statistical/morphological descriptors are provided in the Appendix. The average of the statistical/morphological descriptors $\widehat{f(d)}$ extracted from fifty reconstructed samples is compared with the reference values $f(d)$, based on which the reconstruction error Δf can be measured in the relative $\mathcal{L}_2$-norm:

$$\Delta f = \frac{\left\| \widehat{f(d)} - f(d) \right\|_2}{\|f(d)\|_2} \tag{21}$$

It is noted that all descriptors are computed for the white phase in the bi-phase microstructures.

As to the model training of neural networks in the proposed SLM, the data events collected from 2D training images are split into the training set (80%) and validation set (20%), in order to enhance the model generalization capacity through cross-validation. The parameters of the proposed SLM for different 2D-to-3D reconstruction cases are summarized in Table 1.

Table 1: The parameters in different cases of 2D-to-3D microstructure reconstruction using the proposed SLM

Testing case	Neighbourhood radius (voxels)	Adjustment coefficient β	ANN model training				
			Number of 2D training image(s)	Learning rate	Epoch numbers	Number of neurons	
						Hidden layer 1	Hidden layer 2
Example 1	$r_{xy} = r_{yz} = r_{zx} = 5$	1.0015	1	0.0001	500	60	30
Example 2	$r_{xy} = r_{yz} = r_{zx} = 7$	1.0010	3	0.0001	500	80	40
Example 3	$r_{xy} = r_{yz} = r_{zx} = 15$	0.9995	3	0.0001	800	100	40
Example 4	$r_{xy} = r_{yz} = r_{zx} = 14$	1.0015	3	0.0001	1000	100	50
Example 5	$r_{xy} = 15$	0.9980	1	0.0001	800	100	40
	$r_{yz} = 5$	1.0000	1	0.0001	500	60	20
	$r_{zx} = 5$	1.0000	1	0.0001	500	60	20
Example 6	$r_{xy} = r_{yz} = r_{zx} = 14$	0.9980	3	0.0001	1000	100	40
Example 7	$r_{xy} = r_{yz} = r_{zx} = 14$	1.0000	3	0.0001	1000	200	80

4.1 Example 1: Polymer nanocomposite with low volume fraction of secondary phase

A dielectric polymer nanocomposite consisting of about 1.40% silica (white phase) and 98.60% epoxy is selected as the first representative example. The super high volume ratio between the primary and secondary phase may pose a great challenge to microstructure reconstruction, because the informatics of the secondary phase can be overwhelmed by that of the primary phase at the stage of microstructure characterization via supervised learning.

As shown in Figure 16, the 2D cross-sectional image of limited size is the only graphical information available for 3D reconstruction. With isotropic assumption, SOR, GRFT and SLM are used to generate 3D microstructure samples from it, and representative reconstruction results are presented in Figure 17. The SOR samples are reconstructed through a stochastic optimization process based on the simulated annealing algorithm (Torquato and Yeong, 1998), where the two-point correlation function (Torquato, 2002) extracted from the 2D reference image is set as the optimization objective. After $800,000$ times of voxel value exchange, 3D microstructure samples that are statistically equivalent to the 2D slice are obtained. The GRF samples are reconstructed by truncating the 3D Gaussian random field that is inferred from the 2D reference images (Liang et al.,

Figure 16: The representative 2D cross-sectional image (image size: 200×200 pixels) of a dielectric polymer nanocomposite (Bostanabad et al., 2016a).

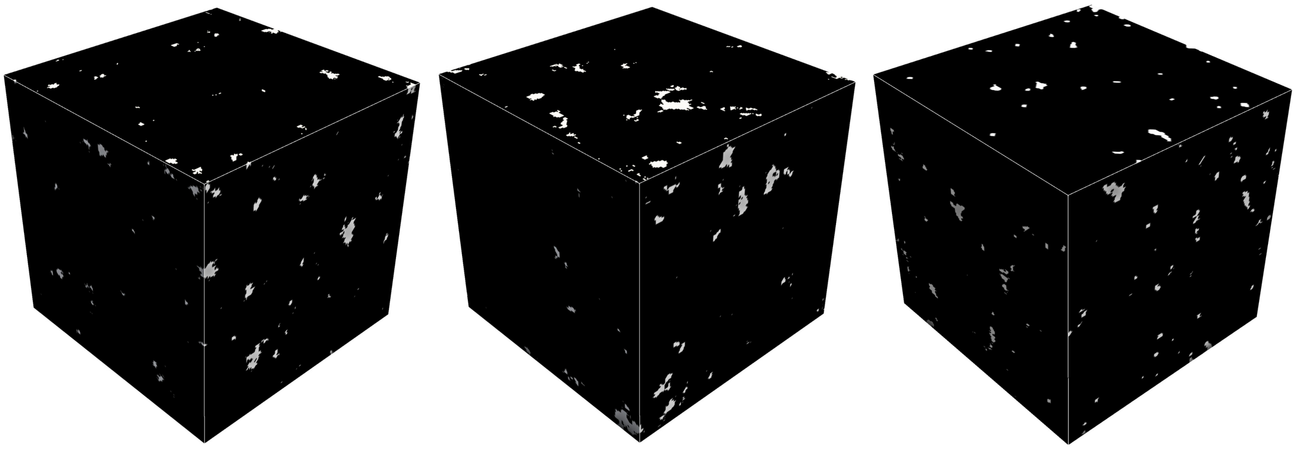

(a) SOR sample I (b) GRFT sample I (c) SLM sample I

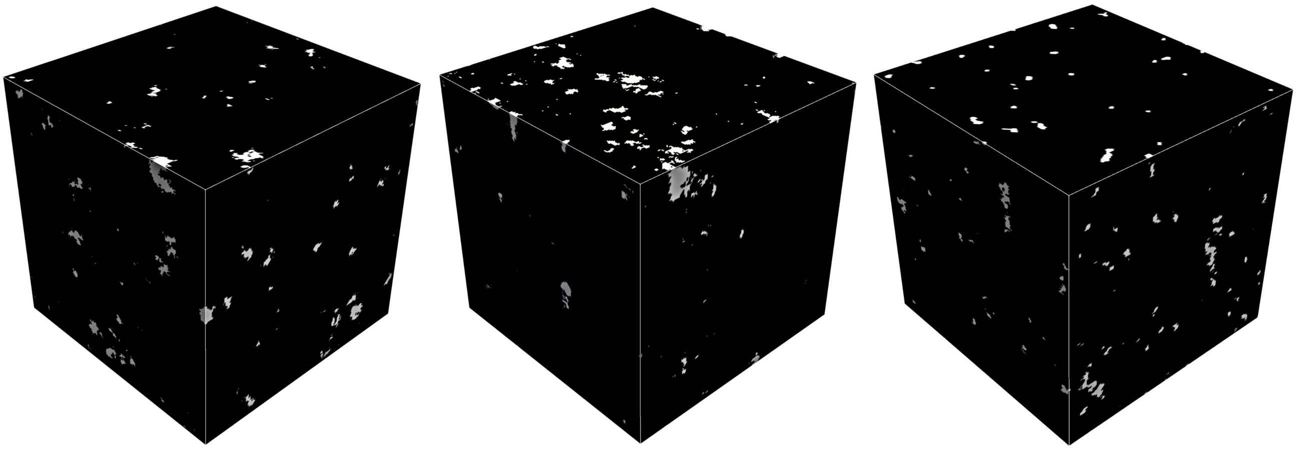

(d) SOR sample II (e) GRFT sample II (f) SLM sample II

Figure 17: The representative results (image size: $200 \times 200 \times 200$ voxels) of different 2D-to-3D microstructure reconstruction methods.

1998), to preserve the first- and second-order statistics. For SLM sample reconstruction, the 2D data template with $r = 5$ pixels is used to capture the elementary features of the 2D slice. A set of ANN models of the same network architecture (with 2 hidden layers, 60 and 30 neurons in the 1st and 2nd layer respectively) are trained, based on which 3D microstructures are synthesized by following the reconstruction procedure in Algorithm 3.

Visual inspection indicates that the SLM samples can well maintain both the irregular geometry and spatial distribution of silica clusters, which are more visually realistic than the SOR and GRFT samples. As illustrated in Figure 18, two-point correlation function $S_2(d)$, lineal path function $L(d)$ and grain size distribution $g(d)$ are extracted from both the 3D reconstructed samples and the 2D reference image, to quantitatively assess the reconstruction quality. It has been proved that the $S_2(d)$ or $L(d)$ curves extracted from the representative 2D and

3D images of the same sample are closely equal (Yeong and Torquato, 1998). However, the $g(d)$ curves extracted from a 2D image is not identical to the one extracted from a 3D image for irregular-shaped grains, which can be understood from the view of stereology. It also explains why the "errors" in Figure 18c are significant, but such "errors" mainly reflect characterization uncertainty due to information asymmetry between 2D and 3D images, rather than the real 2D-to-3D reconstruction errors.

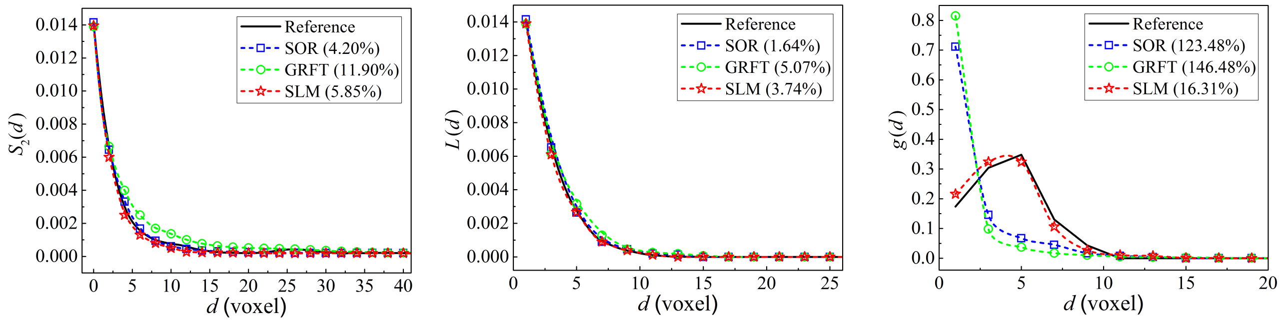

(a) (b) (c)

Figure 18: Comparisons between the 3D reconstructed microstructures and the 2D reference image in terms of (a) two-point correlation function $S_2(d)$, (b) lineal path function $L(d)$ and (c) grain size distribution $g(d)$ (the numbers in parentheses measure the reconstruction errors in relative $\mathcal{L}_2$-norm).

As compared in Figure 18, the good agreements between descriptor curves verify that the proposed SLM can well capture the spatial complexity of the 2D reference image and produce statically and geometrically equivalent 3D microstructure samples. Although the SOR samples exhibit the best performance in preserving $S_2(d)$ and $L(d)$, they fail to maintain the geometrical irregularity of silica grains. The reconstruction accuracy of SOR can be improved by setting complicated or multiple optimization objectives, where more microstructural descriptors such as lineal path function, chord length distribution function and two-point cluster correlation function can be involved in the reconstruction process. On the other hand, the number of iteration steps can also be extended to achieve better SOR results. However, the above operations will dramatically increase the computational intensity of SOR reconstruction. As to the 3D samples reconstructed by GRFT, they can hardly preserve the high-order informatics of the 2D reference image, such as grain size and grain shape, which indicates the inherent limitation of GRFT.

4.2 Example 2: Clustered isotropic microstructure

The second example is also a nanocomposite, which possesses an isotropic microstructure with 9.05% irregularly-shaped silica clusters (white phase) randomly embedded in the rubber matrix (Bostanabad et al., 2016b). As discussed in § 4.1, one representative 2D cross-sectional image is sufficient to fulfil the 3D reconstruction of isotropic microstructures. Here, three representative 2D slices on orthogonal planes are selected from the available 3D reference microstructure, as shown in Figure 16. To test the capacity of SLM in integrating informatics from different directions, all three 2D slices are used as the guidances for 3D microstructure reconstruction.

The SOR samples are generated from simulated annealing optimization procedures after $1,500,000$ iterations, where the (directional) two-point correlation functions extracted three perpendicular slices (in Figure 19) are all involved in the loss function. In GRFT reconstruction, these three 2D cross-sectional images are used separately, which means each directional 2D slice is used as the only guidance to fulfil one-third of the reconstruction task of fifty 3D samples. As to microstructure reconstruction via SLM, the 2D data template with $r = 7$ pixels is selected to capture the primary features of three perpendicular slices, and a set of ANN models of the same size (2 hidden layers with 80 and 40 neural units in the 1st and 2nd layer respectively) are fitted to learn the inherent stochasticity. Following the reconstruction procedure in Algorithm 3, a group of 3D samples are synthesized by integrating 2D morphology patterns.

The representative 3D microstructure samples reconstructed from SOR, GRFT and SLM are presented in Figure 17. It can be easily observed that the SLM samples are much more visually appealing than the SOR and

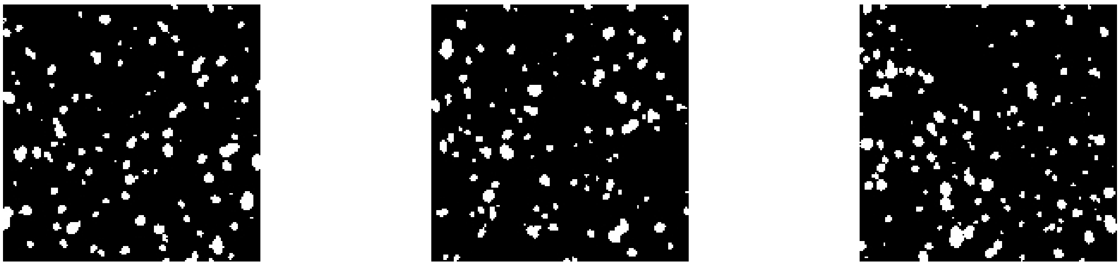
(a) xy-plane (b) yz-plane (c) zx-plane

Figure 19: The representative 2D cross-sectional images (image size: 150×150 pixels) of a clustered isotropic microstructure on three orthogonal planes.

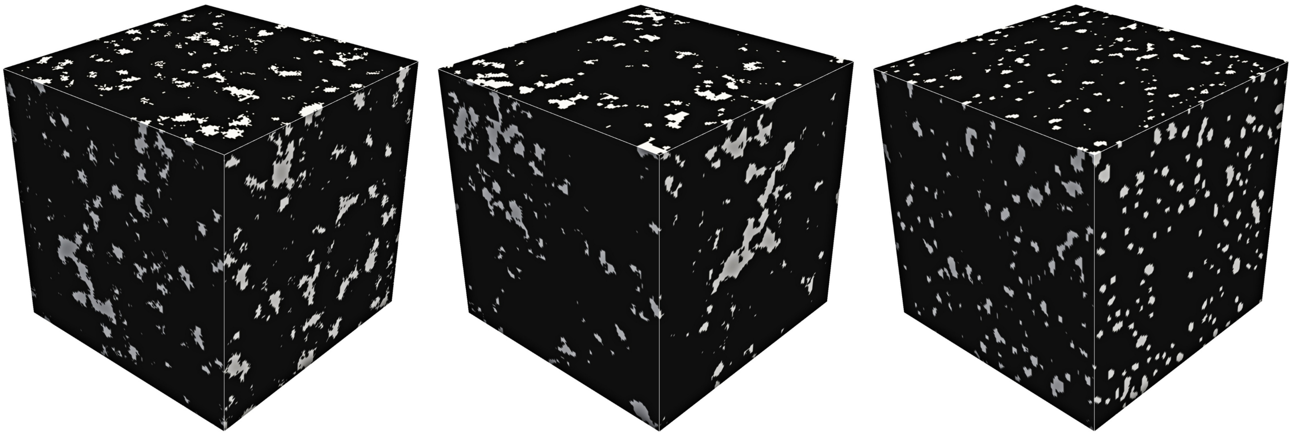
(a) SOR sample I (b) GRFT sample I (c) SLM sample I


(d) SOR sample II (e) GRFT sample II (f) SLM sample II

Figure 20: The representative results (image size: $160 \times 160 \times 160$ voxels) of different 2D-to-3D microstructure reconstruction methods.

GRFT samples. To check the statistical and morphological equivalences, $S_2(d)$, $g(d)$ and two-point cluster correlation function $C_2(d)$ are compared between the 3D reconstructed samples and the 3D reference microstructure, as shown in Figure 21. It takes a great effort for SOR to enforce its reconstructions close to the reference microstructure in the aspect of $S_2(d)$, but microstructural complexities beyond this are not successfully preserved by SOR samples, such as cluster size and shape. Despite the high efficiency of GRFT, it shows poor performance in maintaining the irregular geometry and random spatial distribution of clusters, which can be observed from Figure 21(a) and (b). In addition to the surface appearance, SLM samples are also inherently close to the reference microstructure in all three compared descriptors, which quantitatively verifies the effectiveness of the

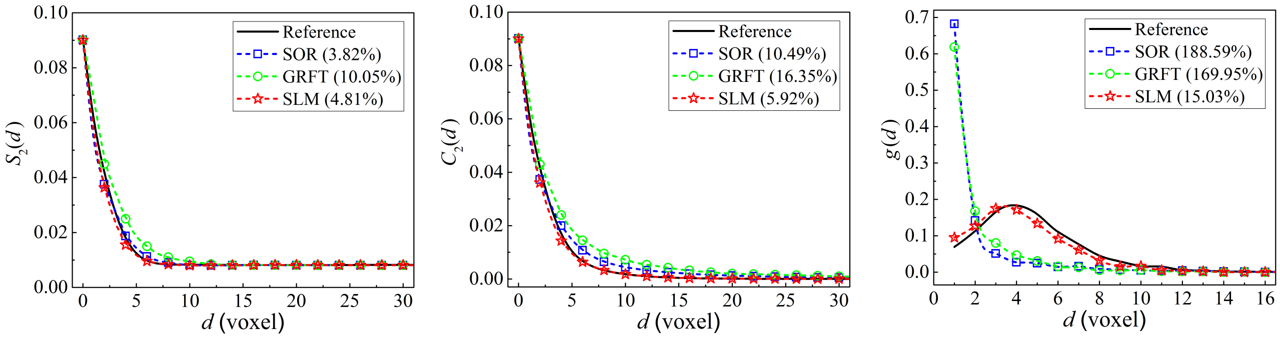

(a) (b) (c)

Figure 21: Comparisons between the 3D reconstructed and reference microstructures in terms of (a) two-point correlation function $S_2(d)$, (b) two-point cluster correlation function $C_2(d)$ and (c) grain size distribution $g(d)$ (the numbers in parentheses measure the reconstruction errors in relative $\mathcal{L}_2$-norm).

new SLM in 2D-to-3D microstructure reconstruction.

4.3 Example 3: Porous media with wide pore size range

Leopard sandstone (Herring et al., 2018) is selected as the typical porous media to test the capacity of SLM in 2D-to-3D reconstruction. Its solid matrix is naturally hollowed out to form a complicated internal microstructure with 13.62% pore space (white phase) occupying the entire volume. The distinctiveness of Leopard sandstone lies in its great variation of pore size, which can be observed from the graphs in Figure 22. To enhance the reconstruction quality, representative 2D slices in three perpendicular directions are used as the information source for 3D microstructure synthesis.

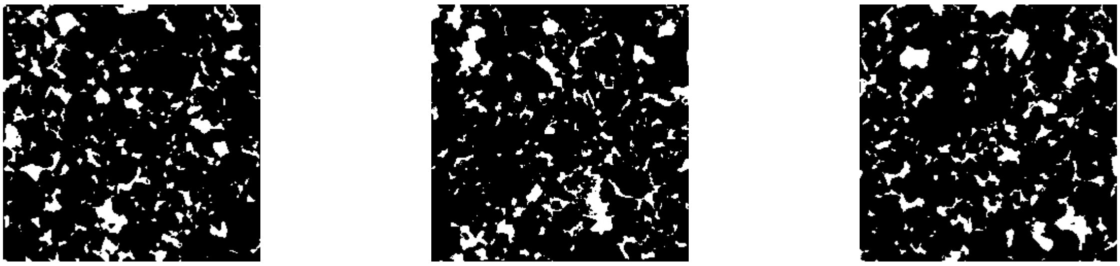

(a) xy-plane (b) yz-plane (c) zx-plane

Figure 22: The representative 2D cross-sectional images (image size: 250×250 pixels) of a Leopard sandstone sample on three orthogonal planes.

As shown in Figure 23, representative 3D samples reconstructed from SOR, GRFT and SLM are put together for visual comparison. Two-point correlation functions of the 2D cross-sectional images are used as the optimization objectives for SOR, and 3D samples are obtained after $1,000,000$ iterative steps. As to microstructure reconstruction using SLM, the 2D data template with $r = 15$ pixels is selected to collect local morphology patterns from training images, and then a set of ANN models with the same architectures (2 hidden layers with 100 and 40 nodes in the 1st and 2nd layer respectively) are trained to statistically characterize microstructural complexities.

As can be observed from Figure 23, the superficial appearance of the SLM samples is much closer to the 2D reference images, compared to the SOR and GRFT samples. To check whether the great variation of pore size is preserved by reconstructed samples, microstructural descriptors including $L(d)$, chord length distribution $\rho(d)$ and pore size distribution $p(d)$, are extracted from both the reconstructed and original 3D microstructures for quantitative comparison. All these three descriptors can provide microstructural characteristics in aspect of pore geometry (size and shape), and the results are given in Figure 24. Obviously, only the SLM samples are

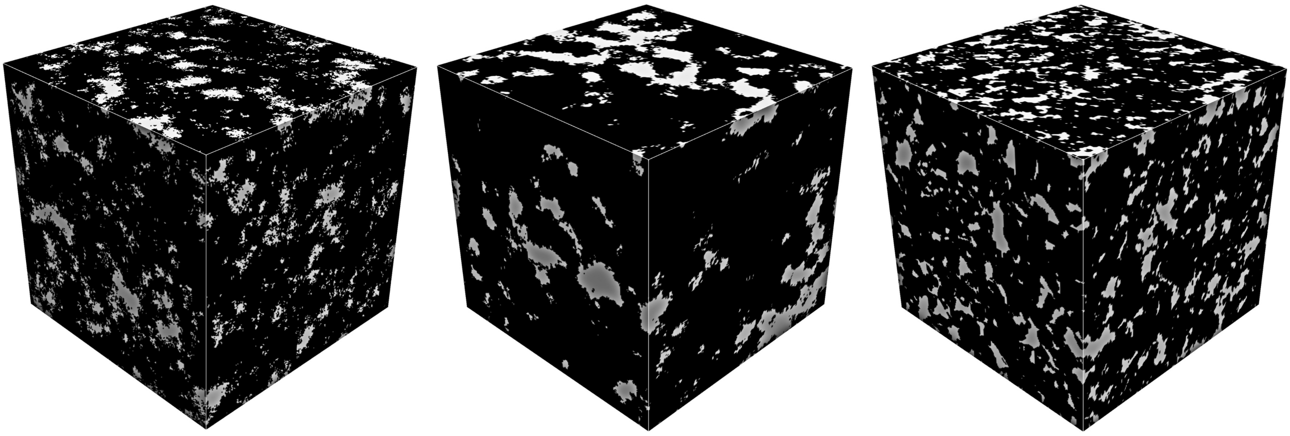

(a) SOR sample I (b) GRFT sample I (c) SLM sample I

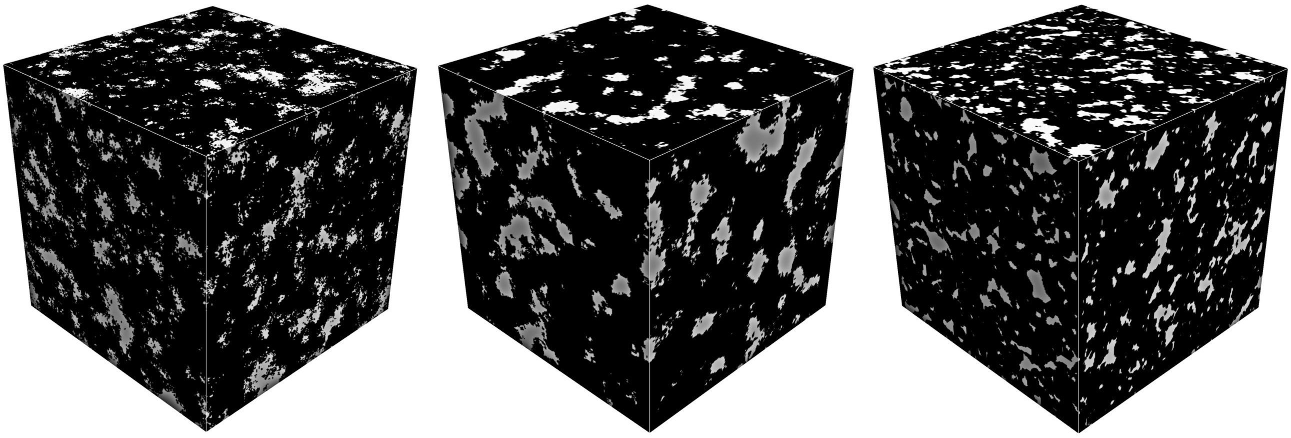

(d) SOR sample II (e) GRFT sample II (f) SLM sample II

Figure 23: The representative results (image size: $250 \times 250 \times 250$ voxels) of different 2D-to-3D microstructure reconstruction methods.

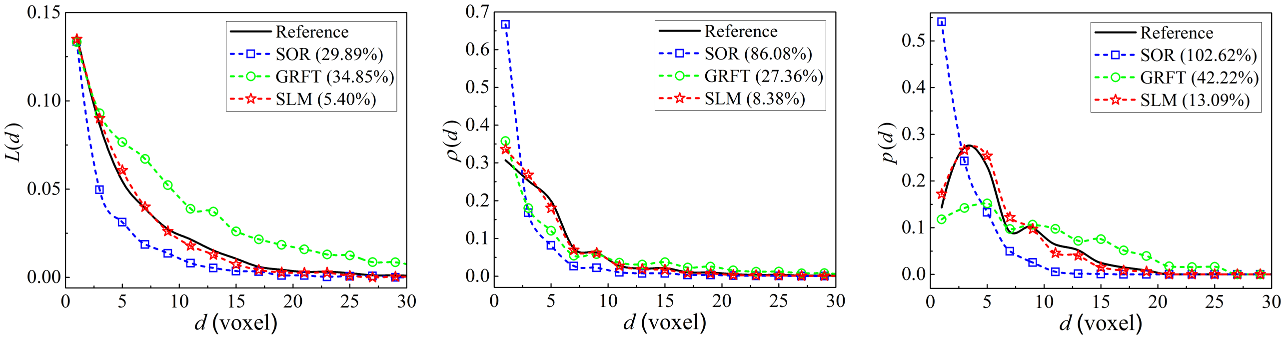

(a) (b) (c)

Figure 24: Comparisons between the 3D reconstructed and reference microstructures in terms of (a) lineal path function $L(d)$, (b) chord length distribution $\rho(d)$ and (c) pore size distribution $p(d)$ (the numbers in parentheses measure the reconstruction errors in relative $\mathcal{L}_2$-norm).

statistically equivalent to the original microstructure in terms of pore geometry, which can be proved by the good matches between descriptor curves. As to the SOR and GRFT samples, the remarkable disagreements between descriptor curves indicate that pore geometry is poorly maintained by these reconstructed samples.

4.4 Example 4: Porous media with long-distance connectivity

In porous media research, Fontainebleau sandstone (Fu et al., 2020a) is often used as the reference standard for validation purpose. Here, a Fontainebleau sandstone sample (Berg, 2016) with porosity equal to 24.50% is chosen to check the general applicability of SLM in reconstructing pore microstructures. As shown in Figure 25, representative 2D slices in three perpendicular directions are taken from the original 3D microstructure. Pore bodies with irregular geometry are linked together to form a far-range percolating network. The main challenge for SLM is to capture the long-distance pore connectivity that is far beyond the size of data templates.

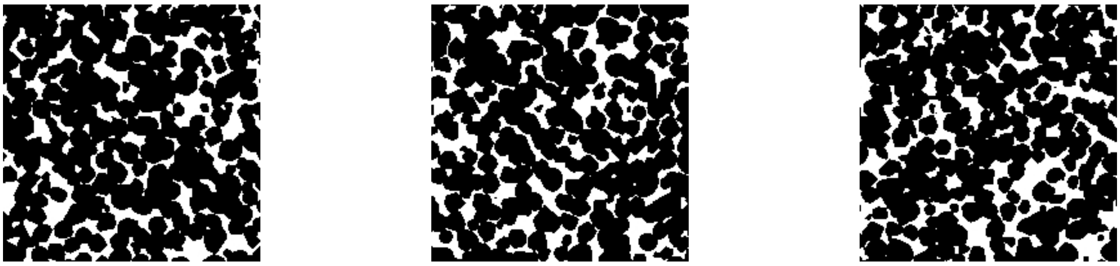

(a) xy-plane (b) yz-plane (c) zx-plane

Figure 25: The representative 2D slices (image size: 200 × 200 pixels) of a Fontainebleau sandstone sample on three orthogonal planes.

Based on the 2D reference images in Figure 25, 3D microstructure samples are reconstructed from SOR, GRFT and SLM respectively, and representative results are shown in Figure 26. The SOR samples are generated through a stochastic optimization procedure after $1,200,000$ iterations, but it seems more iterative steps are still required to refine the reconstruction results. The SLM samples are reconstructed by using the 2D data template with $r = 14$ pixels to characterize the basic features, and a set of ANN models of the same size (2 hidden layers with 100 and 50 neural units respectively) are trained to model the microstructural characteristics.

Visual comparison indicates that only the SLM samples preserve the morphological appearance of the reference images. Quantitative analysis is also conducted by comparing statistical, geometrical and topological attributions between the 3D reconstructed and original microstructures, namely $S_2(d)$, $p(d)$ and total fraction of percolating cells $T_3(L)$. The SOR samples precisely maintain the reference $S_2(d)$ thorough prohibitively expensive optimization procedures, but they are greatly different from the original microstructure in terms of pore geometry, as illustrated in Figure 27(a) and (b), respectively. Microstructural informatics in high order, such as pore size and long-distance connectivity, are beyond the capacity of GRFT, which can be observed from the disagreements of descriptor curves in Figure 27(b) and (c). As to SLM, it is able to generate statistically, geometrically and topologically realistic 3D pore microstructures, which is verified by the good matches between the compared descriptor curves.

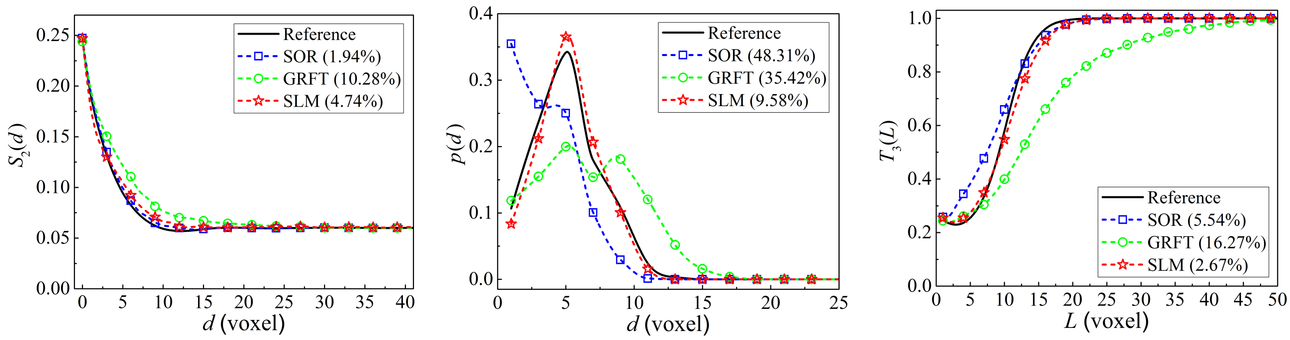

(a) (b) (c)

Figure 27: Comparisons between the 3D reconstructed and reference microstructures in terms of (a) two-point correlation function $S_2(d)$, (b) pore size distribution $p(d)$ and (c) total fraction of percolating cells $T_3(d)$ (the numbers in parentheses measure the reconstruction errors in relative $\mathcal{L}_2$-norm).

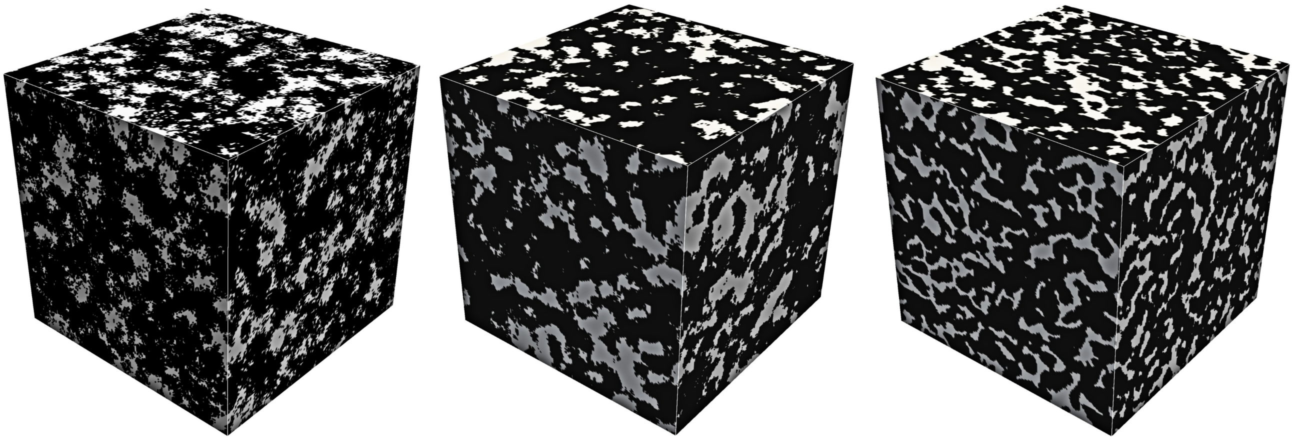

(a) SOR sample I (b) GRFT sample I (c) SLM sample I

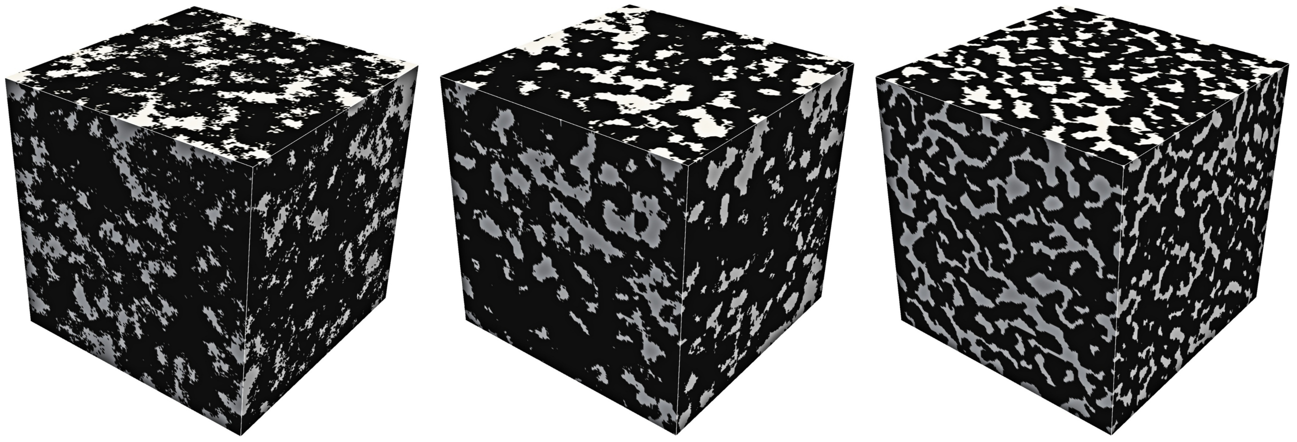

(d) SOR sample II (e) GRFT sample II (f) SLM sample II

Figure 26: The representative results (image size: $200 \times 200 \times 200$ voxels) of different 2D-to-3D microstructure reconstruction methods.

4.5 Example 5: Anisotropic microstructure

In this subsection, the proposed SLM is applied to synthesize 3D anisotropic microstructure samples by using the directional 2D slices with significantly distinct morphologies as the references. As shown in Figure 28, the representative 2D slices are selected from the original 3D microstructure on orthogonal planes. The white phase occupies approximately 39.16% of the bulk volume, and it presents as a stripped texture with long-distance correlation on xy-plane and spotted patterns with irregular geometry on both yz- and zx-planes. Generally, the 2D-to-3D reconstruction of anisotropic microstructures is more challenging than the isotropic reconstruction, because different configurations (such as the size of data templates) are required to be carefully set, so as to capture the basic feature on each plane.

To capture the anisotropic property, the two-point correlation functions in the diagonal direction are extracted from three orthogonal planes, and they are all included into the optimization objectives for the 2D-to-3D microstructure reconstruction via SOR, as presented in Figure 30(a)-(c). To investigate the dependence of SOR reconstruction quality on iteration times, SOR samples are generated after super huge numbers of iterations (i.g. $5,000,000$ times). For SLM reconstruction, data templates with radii $r_{xy} = 15$, $r_{yz} = 5$ and $r_{zx} = 5$ pixels are used to collect data events from xy-, yz- and zx-planes receptively, so as to take account of morphology differences on orthogonal planes. Based on the collected training data, three sets of ANN models $\boldsymbol{M}_{(r)}^{(xy)}$ (with 2 hidden layers, 100 and 40 neurons in the 1st and 2nd layer respectively), $\boldsymbol{M}_{(r)}^{(yz)}$ (with 2 hidden layers, 60 and 20 neurons in the 1st and 2nd layer respectively), and $\boldsymbol{M}_{(r)}^{(zx)}$ (with 2 hidden layers, 60 and 20 neurons in the 1st and

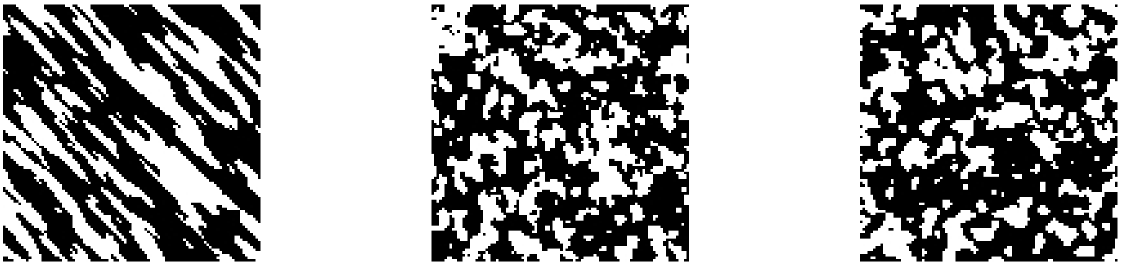

(a) xy-plane (b) yz-plane (c) zx-plane

Figure 28: The representative 2D slices (image size: 100×100 pixels) of the anisotropic microstructure on three orthogonal planes.

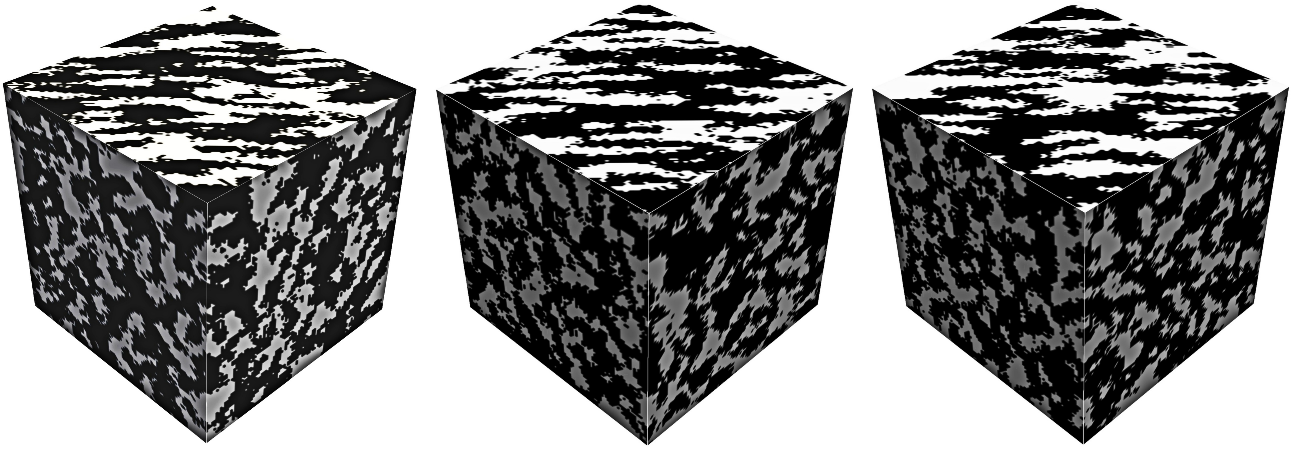

(a) SOR sample I (b) SOR sample II (c) SOR sample II

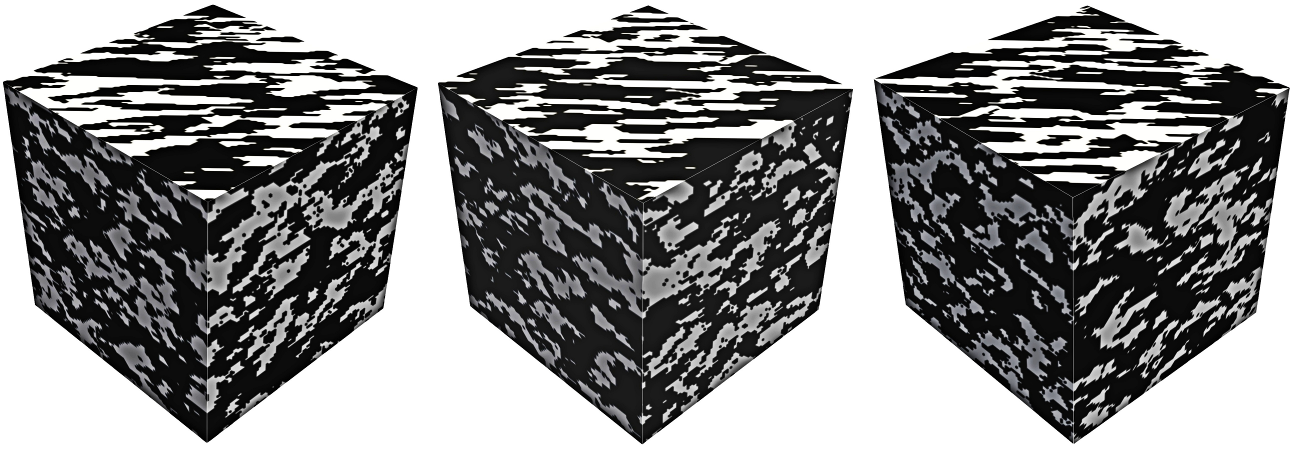

(d) SLM sample I (e) SLM sample II (f) SLM sample III

Figure 29: The representative results (image size: $100 \times 100 \times 100$ voxels) of different 2D-to-3D microstructure reconstruction methods.

2nd layer respectively) are fitted to characterize the basic feature on each plane, as well as to capture the overall isotropic property. As to GRFT, it is not used here for the 2D-to-30 reconstruction of isotropic microstructures.

Representative samples reconstructed from SOR and SLM are shown in Figure 29, from which one can observed that both the SOR samples and the SLM samples are closely similar to the 2D reference images. Reconstruction accuracy is quantitatively evaluated by comparing statistical/morphological descriptors between the 3D reconstructed and original microstructures, and the results are provided in Figure 30. The good agreements between $S_2(d)$ curves in three orthogonal directions indicate that both the SOR and SLM samples well preserve

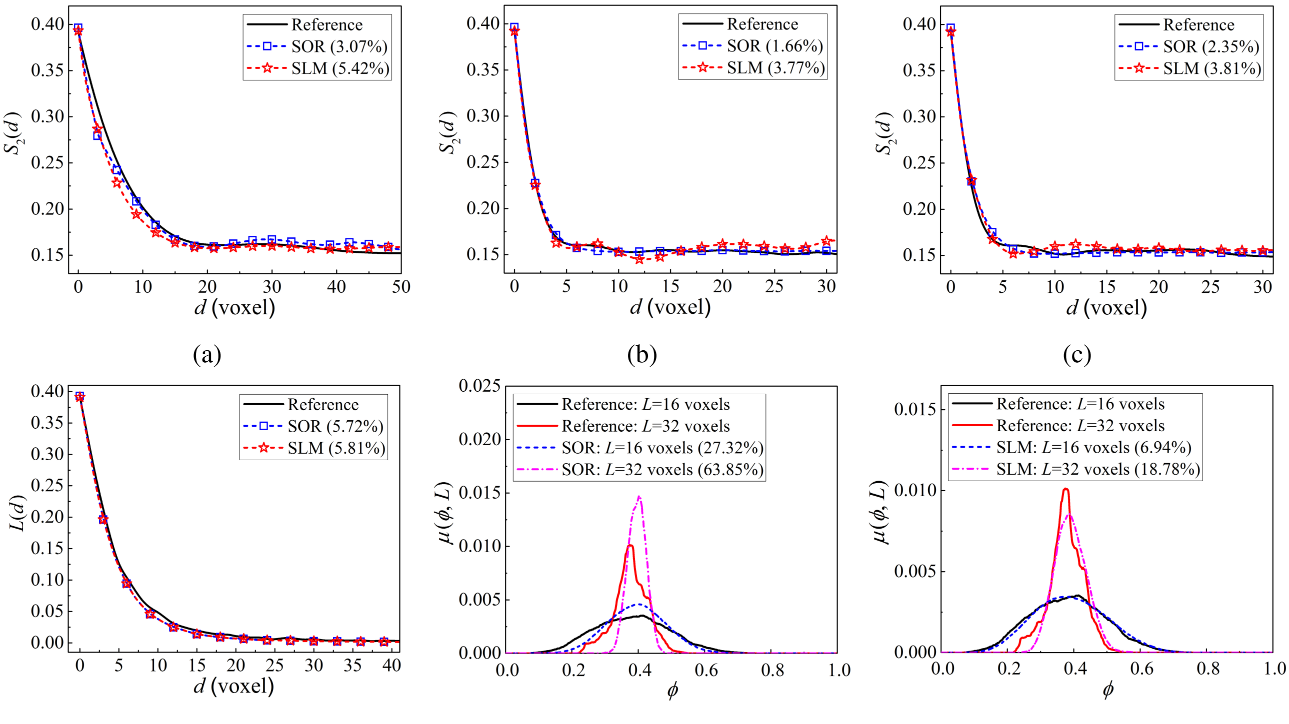

(a) (b) (c)

(d) (e) (f)

Figure 30: Comparisons between the 3D reconstructed and reference microstructures in terms of (a) directional two-point correlation function $S_2(d)$ (xy-plane-45°), (b) $S_2(d)$ (yz-plane-45°), (c) $S_2(d)$ (zx-plane-45°), (d) lineal path function $L(d)$, (e) local volume fraction distribution $\mu(\phi, L)$ (SOR samples) and (f) $\mu(\phi, L)$ (SLM samples) (the numbers in parentheses measure the reconstruction errors in relative $\mathcal{L}_2$-norm).

the anisotropic property of the original microstructure, as can be seen in Figure 30(a)-(c). After putting extremely high expense in optimization, the SOR samples exhibit a slightly higher accuracy than the SLM samples in aspects of $S_2(d)$ and $L(d)$. But when it comes to local volume fraction distribution $\mu(\phi, L)$, SLM shows better performance than SOR, which can be observed from Figure 30(e) and (f). In summary, the developed SLM is capable to create 3D isotropic microstructures that are statistically and morphologically equivalent to the original microstructure.

4.6 Example 6: Synthetic silica with high porosity

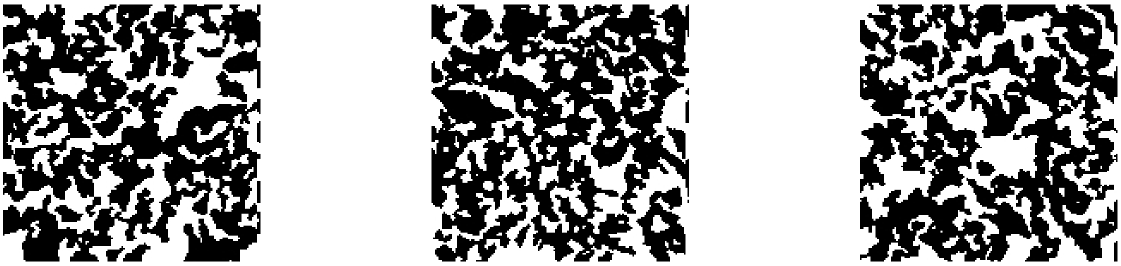

(a) xy-plane (b) yz-plane (c) zx-plane

Figure 31: The representative 2D slices (image size: 150×150 pixels) of the synthetic silica on three orthogonal planes.

The sixth example is a synthetic media (Dong, 2008) with pore space (white phase) and silica skeleton occupying about 42.50% and 57.50% of the entire volume respectively. Representative 2D slices are selected from three orthogonal planes inside the 3D silica microstructure, as shown in Figure 31. Compared to Examples 4.3

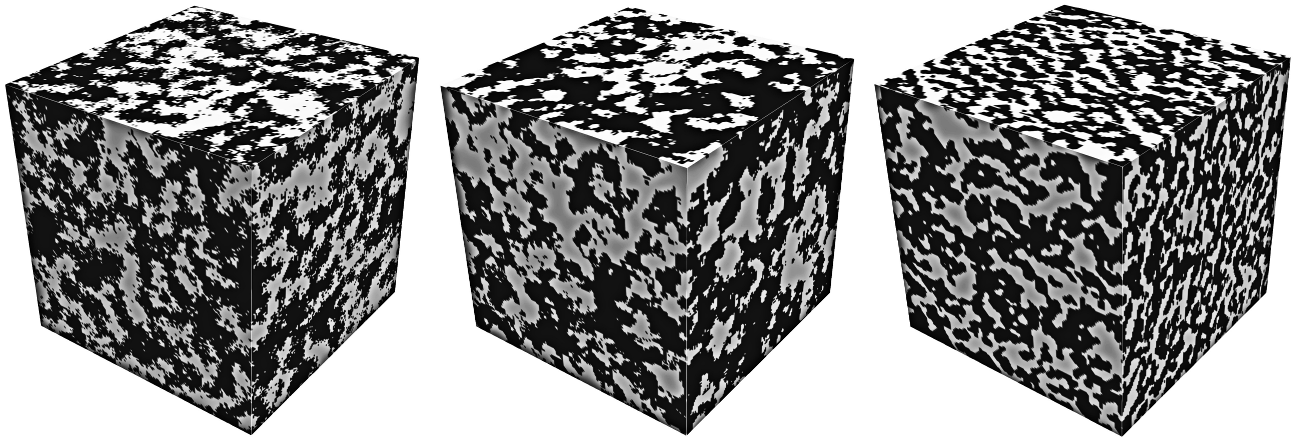

(a) SOR sample I (b) GRFT sample I (c) SLM sample I

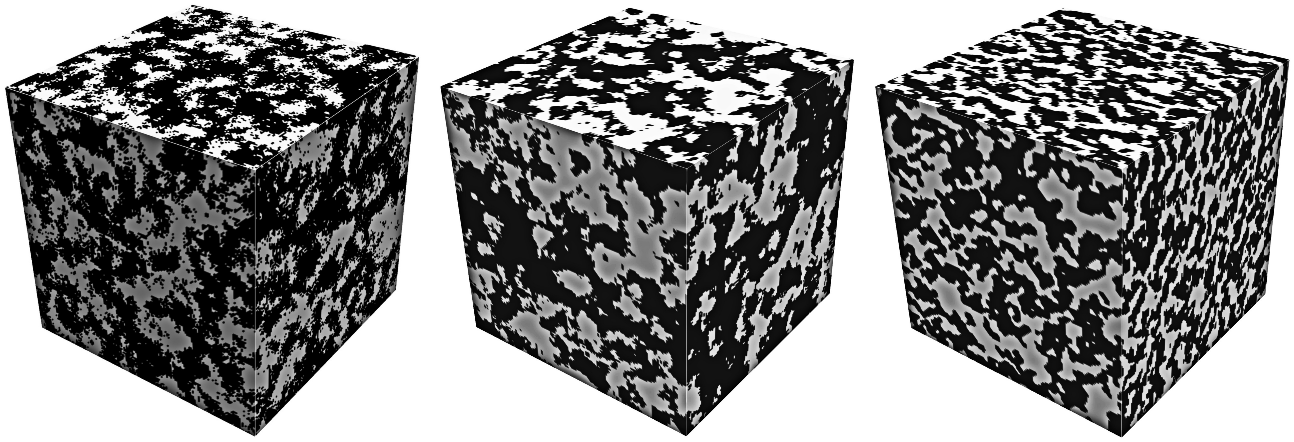

(d) SOR sample II (e) GRFT sample II (f) SLM sample II

Figure 32: The representative 3D samples (image size: $160 \times 160 \times 160$ voxels) obtained from different 2D-to-3D microstructure reconstruction methods.

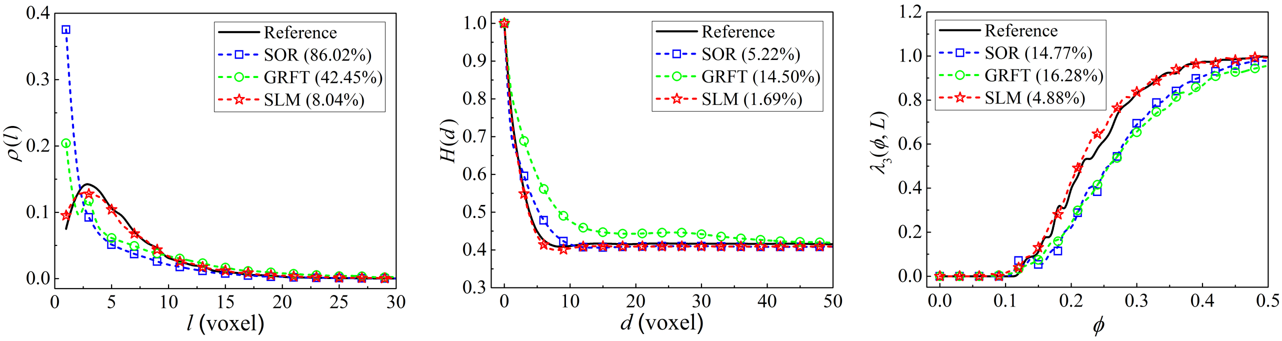

(a) (b) (c)

Figure 33: Comparisons between the 3D reconstructed and reference microstructures in terms of (a) chord length distribution $\rho(d)$, (b) pair connectivity function $H(d)$ and (c) local percolation probabilities $\lambda_3(\phi, L)$ (L=12 voxels) (the numbers in parentheses measure the reconstruction errors in relative $\mathcal{L}_2$-norm).

and Example 4.4, the volume fraction and connectivity range of the pore space in this example are significantly higher, which may require more complicated models to capture the long-range features and inherent stochasticity. To enhance the reconstruction accuracy, the 2D slice on three orthogonal planes are used together as the references for the 3D isotropic reconstructions via SOR, GRFT and SLM.

The SOR samples are obtained from the simulated annealing procedure after $1,500,000$ times of voxel value exchange. For SLM reconstruction, data templates with radii $r_{xy} = r_{yz} = r_{zx} = 14$ pixels are used to collect local morphology patterns from the training images, and then a set of ANN models of the same network architecture (2 hidden layers with 100 and 40 neurons on the 1st and 2nd layer respectively) are trained for stochastic microstructure characterization. As shown in Figure 32, representative 3D reconstruction results obtained from SOR, GRFT and SLM are given. It can be easily observed that the SLM samples are more visually similar to the 2D reference images, compared to the SOR and GRFT samples.

Microstructural descriptors, including chord length distribution $\rho(l)$, pair connectivity function $H(d)$ and local percolation probabilities $\lambda_3(\phi, L)$, are used to evaluate the reconstruction accuracy, as demonstrated in Figure 33. The SOR and GRFT samples are greatly different from the original microstructure in aspects of $\rho(l)$ and $\lambda_3(\phi, L)$, which means they fail to preserve the pore geometry and percolation information. Besides, GRFT also exhibits poor performance in capturing the poor connectivity. The SLM samples closely resemble the original microstructure in terms of pore size, pore connectivity and local variation of pore percolation, which can be verified by the good agreements between descriptor curves.

4.7 Example 7: Multiphase porous electrode microstructure

To examine the performance of the proposed SLM on multiphase materials, a porous electrode microstructure with three distinct phases is selected as the seventh testing example, as shown in Figure 34. The blue, green and red phases of this porous medium are yttria stabilized zirconia (YSZ), Nickel and pore space, respectively (Lu et al., 2017). All three phases possess complicated geometry and are distributed randomly in space. Because SOR and GRFT are mainly used for bi-phase microstructure reconstruction, here only the proposed SLM is applied to generate 3D multiphase microstructures by using 2D training images.

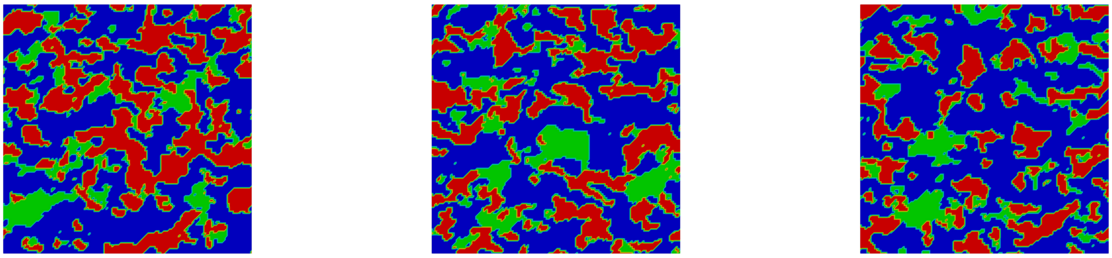

(a) xy-plane (b) yz-plane (c) zx-plane

Figure 34: The representative 2D slices (image size: 150×150 pixels) of the multiphase porous electrode microstructure on three orthogonal planes.

The blue phase has the largest correlation length, and its value is equal to 13.7 pixels, which can be directly measured from the two-point correlation curves shown in Figure 36. Therefore, the 2D data templates with radii $r_{xy} = r_{yz} = r_{zx} = 14$ pixels are used to collect data events, in order to cover the primary morphological features present in the training images. Compared to the above bi-phase microstructures, this triple-phase microstructure requires a more complicated ANN model to statistically characterize the microstructural complexities. A set of ANN models with the same network architecture (2 hidden layers with 200 and 80 neurons on the 1st and 2nd layer respectively) are fitted to learn the local morphology patterns. More details about ANN model training are provided in Table 1.

Three representative 3D microstructures reconstructed by SLM are shown in Figure 36. Visual inspection indicates that the 3D reconstructed microstructures well preserve the morphology appearances of the 2D training images. To quantitatively assess the reconstruction quality, statistical descriptors including two-point correlation function $S_2(d)$, lineal path function $L(d)$ and chord length function $\rho(d)$ are extracted from the 3D reconstructed and the reference microstructures. These descriptors are computed for all three phases of this porous electrode microstructure, and the results are plotted in Figure 36. The relative $\mathcal{L}_2$-norm errors of the statistical descriptors are all around 5.00%, and the good agreement confirms that the proposed SLM is capable to generate 3D multiphase microstructures statistically equivalent to the 2D training images.

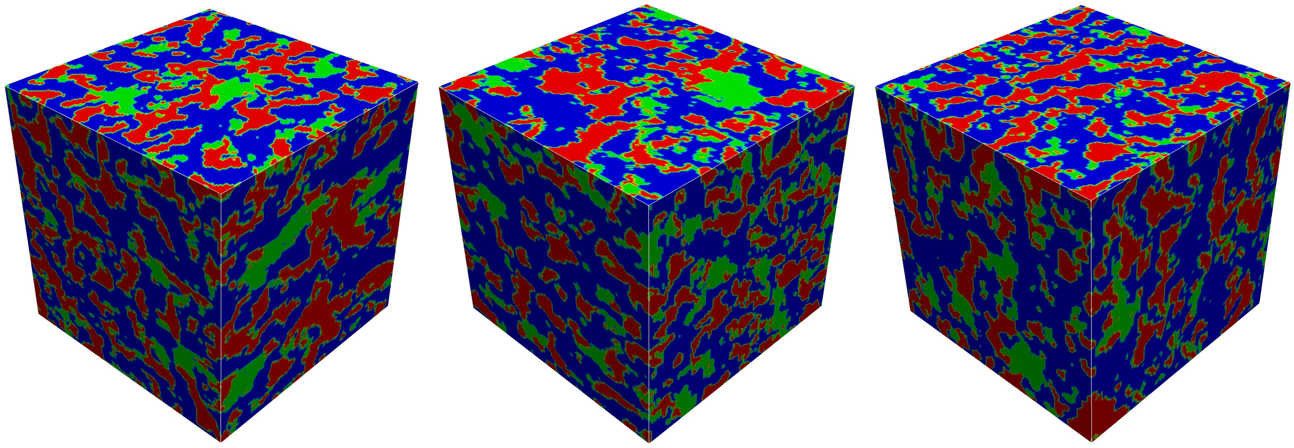

(a) SLM sample I (b) SLM sample II (c) SLM sample II

Figure 35: The representative 3D samples (image size: $150 \times 150 \times 150$ voxels) obtained from the proposed SLM.

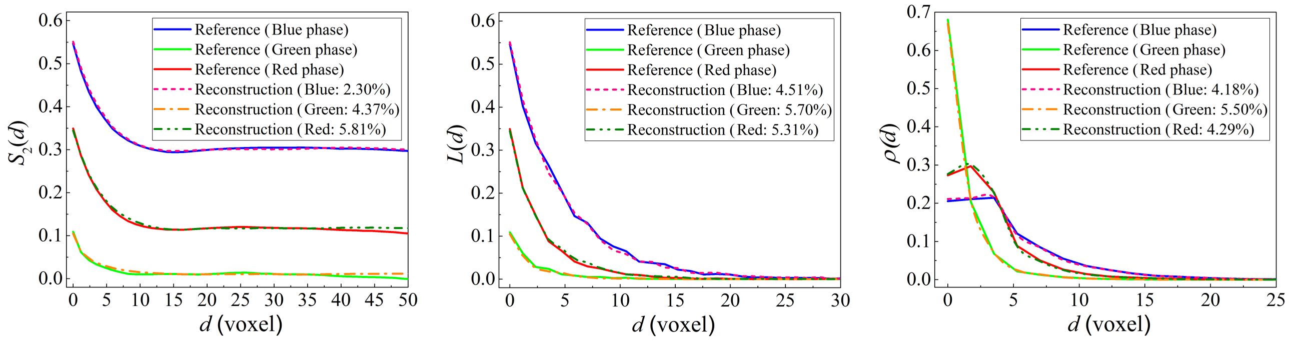

(a) (b) (c)

Figure 36: Comparisons between the 3D reconstructed and reference microstructures in terms of (a) Two-point correlation function $S_2(d)$, (b) lineal path function $L(d)$, and (c) chord length distribution $\rho(d)$ (the numbers in parentheses measure the reconstruction errors in relative $\mathcal{L}_2$-norm).

5 Discussion and conclusions

5.1 Discussion

In § 4, a comprehensive comparison has been conducted between SOR, GRFT and the novel SLM, in terms of 2D-to-3D reconstruction quality. In practice, efficiency is the other important performance index to assess the effectiveness of a microstructure reconstruction method, which indicates the time cost to generate a complete computation ensemble covering all possible configurations. In this study, all these three methods are implemented using MATLAB. Microstructure reconstructions of the seven testing examples are all run on the ASTUTE 2020 HPC cluster in Swansea University (72 nodes, 2 × 14 core CPUs per node, 64 GB RAM per node), and the average computation cost of each reconstruction case is recorded in Table 2.

Microstructure reconstruction can be roughly categorized into field-based and voxel-based methods. As a typical field-based method, GRFT considers heterogeneous media as random fields and generates new samples through field transformation, which explains why GRFT possesses such high efficiency. In contrast, SOR and the proposed SLM are much slower than GRFT, because they fall into the voxel-based category that constructs new samples by iteratively determining voxel's value one by one. SOR needs to repeatedly characterize the intermediate result at each iteration step, while the new SLM just requires to quickly extract statistical characteristics from the pretrained machine learning model(s) for generating each voxel, which is the main reason why SLM

Table 2: Computational costs of microstructure reconstructions using different methods

Testing case	Image size (voxels)	Average CPU time cost (s)			
		SOR	GRFT	**SLM**	
				Characterization (ANN model training)	Reconstruction
Example 1	200 × 200 × 200	674703.9	341.3	25.3	6099.8
Example 2	160 × 160 × 160	641881.6	147.5	65.7	3747.7
Example 3	250 × 250 × 250	1513560.4	794.8	324.5	12105.1
Example 4	200 × 200 × 200	1023482.8	278.7	279.0	6648.8
Example 5	100 × 100 × 100	67644.8	–	214.1	580.9
Example 6	160 × 160 × 160	641203.2	144.8	187.7	4254.6
Example 7	150 × 150 × 150	–	–	246.5	3860.0

is one hundred and more times faster than SOR. As recorded in Table 2, the supervised machine learning-based characterization can be also quickly completed in minutes, and once properly trained, these machine learning models can be stored for repeated usage.

As listed in Table 2, it takes days, even weeks to generate a 3D REV sample using SOR, which is usually unaffordable for data-driven modelling in computational material science or earth science that requires a large number of newly reconstructed samples. The reconstruction quality of SOR strongly depends on the predefined optimization objective and the number of iteration times. GRFT is able to create a 3D REV sample in minutes, but its reconstruction quality is far from adequate for subsequent microstructure analyses. As comprehensively compared in § 4, a series of testing examples have demonstrated that SLM has the best performance in capturing microstructural characteristics far beyond low-order statistics. According to Table 2, SLM only requires one to three hours to produce a 3D REV sample by preserving the statistical equivalences, geometrical complexities, topological attributes and morphological similarities of the reference microstructures. Therefore, the proposed SLM is an accurate, cost-effective and robust method for stochastic 2D-to-3D reconstruction, and the reconstructed microstructure samples are sufficiently realistic for further applications in material and earth science.

However, the proposed SLM approach is not without limitation. Firstly, 2D cross-sectional images can not completely represent the corresponding 3D microstructures, therefore, how to select representative 2D slice(s) as the training image(s) is a critical first step to reconstruct equivalent 3D microstructure samples. Secondly, due to the adoption of MRF assumption to model heterogeneous microstructures, the new method may have limitations in capturing global and non-stationary microstructure characteristics. Thirdly, the image post-processing in SLM may bring a certain degree of distortion to reconstruction results, but currently, it is an indispensable step for 3D reconstruction based on incomplete 2D information. Fourthly, the proposed method constructs 3D microstructure samples through a layer-by-layer procedure, which may lead to inconsistency between vertical and horizontal direction and thus introduce artificial anisotropy. Finally, it is not clear that to what extent the new method can generate 3D samples that are statistically equivalent to the reference microstructure in terms of physical properties, including mechanical, hydraulic, diffusional, electrical and thermal properties. The above unanswered questions are all worth further investigating, so as to improve microstructure reconstruction quality.

5.2 Conclusions

The main contribution of this work is to present a novel 2D-to-3D microstructure reconstruction method by using machine learning-based characterization. The proposed method starts by collecting data events from the 2D training image(s), and these data events are then used to train supervised machine learning models to learn the inherent stochasticity for microstructure characterization purposes. A morphology integration scheme is developed to bridge the gap between 2D characterization and 3D reconstruction, where 2D morphological statistics on three orthogonal planes are integrated into the morphological statistics in 3D space. By using the statistical characteristics stored in the fitted machine learning models, new equivalent 3D microstructures can be reconstructed through sequential probability sampling.

In essence, the pretrained supervised machine learning model is an implicit representation of conditional probability distribution function (CPDF) that stochastically characterizes local morphology patterns of the training image(s). For isotropic microstructures, one representative 2D slice is sufficient to serve as the training image, while for anisotropic microstructures, representative 2D slices on three orthogonal planes are required for the machine learning-based characterization. As to the 3D microstructure reconstruction, it is a layer-to-layer construction procedure, where voxels on each layer are generated one by one in the raster scan order. The continuity and connectivity between adjacent layers can be well maintained by the developed scheme of morphology integration.

A comprehensive comparison between the proposed SLM and classic methods is conducted based on a series of testing examples. The new method shows good applicability to various random microstructures with distinct morphologies, and it also exhibits great superiority over classic methods including SOR and GRFT, in terms of reconstruction accuracy and efficiency. Various statistical/morphological descriptors are used to quantitatively evaluate reconstruction quality. For all testing cases, the proposed method possesses the best performance in preserving microstructural complexities, including statistical characteristics, geometrical irregularity, long-distance connectivity and anisotropy. Compared to SOR and GRFT, the proposed SLM is also more cost-effective to generate statistically, geometrically, morphologically and topologically realistic 3D microstructure samples of representative volumes, thereby better supports subsequent studies such as numerical simulation and data-driven modelling.

Acknowledgements

The authors would like to thank the support from China Scholarship Council (CSC Number: 201608440279), Swansea University (Zienkiewicz Scholarship), the Royal Society (Ref.: IEC\NSFC\191628) and the EPSRC grant PURIFY (Ref.: EP\V000756\1).

Appendix: Morphological/statistical descriptors

Two-point correlation function

Two-point correlation function $S_2(\mathbf{r}_1, \mathbf{r}_2)$ (Torquato, 2013) depicts the probability of finding two points located at $\mathbf{r}_1$ and $\mathbf{r}_2$ in the phase of interest:

$$S_2(\mathbf{r}_1, \mathbf{r}_2) = S_2(\Delta\mathbf{r}) = \langle X(\mathbf{r}_1)X(\mathbf{r}_2)\rangle \tag{22}$$

where $\Delta\mathbf{r} = \mathbf{r}_2 - \mathbf{r}_1$, the angular brackets denote the ensemble averaging, and the meaning of $X(\mathbf{r})$ can be found in Eq. (1). For the statistically homogeneous and isotropic media, $S_2(\Delta\mathbf{r})$ only depends on the magnitude of separation distance d, given by

$$S_2(\Delta\mathbf{r}) = S_2(d) \tag{23}$$

where $d = |\Delta\mathbf{r}|$. Two-point correlation function $S_2(d)$ has the significant properties as follows:

$$\begin{aligned} &S_2(d = 0) = \phi \\ &\lim_{d\to\infty} S_2(d) = \phi^2 \end{aligned} \tag{24}$$

where ϕ denotes the volume fraction of the phase of interest.

Two-point cluster correlation function

As an analogue of $S_2(\mathbf{r}_1, \mathbf{r}_2)$, two-point cluster correlation function $C_2(\mathbf{r}_1, \mathbf{r}_2)$ (Torquato, 2013) is defined as the probability of finding two points located at $\mathbf{r}_1$ and $\mathbf{r}_2$ in the same cluster of the phase of interest. Compared to $S_2(\mathbf{r}_1, \mathbf{r}_2)$, $C_2(\mathbf{r}_1, \mathbf{r}_2)$ contains information of cluster size and topological connectivity. The relationship between $S_2(\mathbf{r}_1, \mathbf{r}_2)$ and $C_2(\mathbf{r}_1, \mathbf{r}_2)$ is interpreted by decomposing $S_2(\mathbf{r}_1, \mathbf{r}_2)$ into a connected part and a disconnected part:

$$S_2(\mathbf{r}_1, \mathbf{r}_2) = C_2(\mathbf{r}_1, \mathbf{r}_2) + E_2(\mathbf{r}_1, \mathbf{r}_2) \tag{25}$$

where $E_2(\mathbf{r}_1, \mathbf{r}_2)$ denotes the probability of finding two points at positions $\mathbf{r}_1$ and $\mathbf{r}_2$ in different clusters. Similarly, $C_2(\mathbf{r}_1, \mathbf{r}_2)$ only depends on the magnitude of separation distance d for the statistically homogeneous and isotropic media, given by

$$C_2(\mathbf{r}_1, \mathbf{r}_2) = C_2(\Delta\mathbf{r}) = C_2(d) \tag{26}$$

where $d = |\mathbf{r}_2 - \mathbf{r}_1| = |\Delta\mathbf{r}|$.

Grain orientation distribution

Grain orientation is defined as the direction of the major ellipse axis with respect to the horizontal-rightward direction (Farrell and Healy, 2017; Gao et al., 2020). The angle θ between the major axis and x-axis can range from $-90°$ to $90°$, and grain orientation distribution $\omega(\theta)$ is calculated as the occurrence frequency of θ:

$$\omega(\theta) = \frac{N(\theta)}{N} \quad (-90° \leq \theta \leq 90°) \tag{27}$$

where $N(\theta)$ is the occurrence time of grains with orientation between θ and $\theta + \mathrm{d}\theta$, and N is the total number of grain bodies. The sum of this probability is equal to 1, given by:

$$\int_{-90°}^{90°} \omega(\theta)\mathrm{d}\theta = 1 \tag{28}$$

Lineal path function

For statistically homogeneous and isotropic media, lineal path function $L(d)$ (Torquato, 2013) provides the probability that a line segment with length d wholly falls inside the phase of interest, when randomly casting it into the analyzed medium. For the line segment with length $d \to 0$, $L(d)$ reduces to the probability of finding a point in the phase of interest. As to the line segment with large length, $L(d)$ decays to zero rapidly.

$$\begin{aligned} &L(d = 0) = \phi \\ &\lim_{d \to \infty} L(d) = 0 \end{aligned} \tag{29}$$

Besides, $L(z)$ is considered to contain a certain degree of topological connectedness information, and it can also be used to estimate pore size information.

Chord length distribution

Throwing an infinitely long line into a tested medium, it will be intersected into line segments by the interface of different phases, and the line segments lying in phase of interest are called chords. For statistically homogeneous and isotropic media, chord length distribution function $\rho(d)$ (Torquato, 2013) is defined as the probability of finding a chord with the length between d and $d + \mathrm{d}d$ completely lying inside the phase of interest. Pore size distribution can also be estimated from chord length distribution.

Pair connectivity function

Pair connectivity function $H(\mathbf{r}_1, \mathbf{r}_2)$ (Schlüter and Vogel, 2011) is defined as the probability of two points $\mathbf{r}_1$ and $\mathbf{r}_2$ are linked by a continuous path within the phase of interest P, given by

$$H(\mathbf{r}_1, \mathbf{r}_2) = \mathrm{Prob}\{\mathbf{r}_1 \leftrightarrow \mathbf{r}_2,\ \mathbf{r}_2 \in P | \mathbf{r}_1 \in P\} \tag{30}$$

where $\mathbf{r}_1 \leftrightarrow \mathbf{r}_2$ means the points $\mathbf{r}_1$ and $\mathbf{r}_2$ are connected. This connectivity measurement combines the concept of connected path used in percolation theory with the well-established lag-dependence. For the statistically homogeneous and isotropic media, $H(\mathbf{r}_1, \mathbf{r}_2)$ only depends on the magnitude of separation distance d, given by:

$$H(\mathbf{r}_1, \mathbf{r}_2) = H(\Delta\mathbf{r}) = H(d) = \frac{C_2(d)}{\phi} \tag{31}$$

where $d = |\mathbf{r}_2 - \mathbf{r}_1|$ again.

Pore size distribution

It is usually difficult to define the "pore body" inside porous media with complicated geometries, and there is no uniformity of pore size distribution $p(d)$ (PSD) (Münch and Holzer, 2008). Due to the mathematically unambiguous definitions of PSD, several image analysis methods have been developed to extract PSD from images, including the intercept method, the random point method, the pore skeleton method, the discrete method, the continuous method and the morphological opening method. Only the discrete method and the morphological opening method are used to evaluate microstructure reconstruction quality in this study.

The entire pore network system can be split into discrete objects based on a specific criterion, and then equivalent pore diameters d_{eq} are derived from the areas (2D) or the volumes (3D) of the discrete pore bodies (Münch and Holzer, 2008). However, there is a lack of reliable methods to recognize individual pore objects, and the splitting process may introduce significant uncertainties to the determination of PSD. Here, the watershed algorithm is adopted to partition the pore network, and the discrete PSD $p(d)$ is then calculated in a histogram form to represent the empirical probability density of pore diameter.

PSD $p(d)$ can also be determined through a morphological opening process, where a successive morphological opening is performed on the pore space with a circular or spherical structuring element (SE) of increasing size (Taiwo et al., 2016). After each opening operation, the resulting pore space only preserves the pores larger than the SE with a specific radius. The opening operation is repeated with increasing SE size until the entire pore space vanishes. The pore volume fraction with a specific radius can be calculated from the difference of pore volumes between two successive opening steps, so as to estimate the PSD $p(d)$. The obtained pore radius is equivalent to the radius of the maximum inscribed circle or sphere inside the pore.

Grain size distribution

Grain size distribution $g(d)$ (GSD) (Buscombe, 2008; Rabbani and Ayatollahi, 2015) can be determined by using the same methods of PSD. Here, the discrete method and the morphological opening method are used to quantitatively assess microstructure reconstruction accuracy.

Local porosity (volume fraction) distribution

Local porosity (volume fraction) distribution (Hilfer, 2002) is to measure local porosities from compact subsets of a porous medium and collect the measurements in a histogram form to represent the empirical probability density. A measurement cell $K(\mathbf{r}, L)$ is defined as a cube (or a square) with side-length L centered at the position $\mathbf{r}$ inside the porous medium, and local porosity $\phi_{\mathrm{local}}(\mathbf{r}, L)$ is defined as the porosity of this measurement cell $K(\mathbf{r}, L)$:

$$\phi_{\mathrm{local}}(\mathbf{r}, L) = \frac{V(P \cap K(\mathbf{r}, L))}{V(K(\mathbf{r}, L))} \tag{32}$$

where P denotes pore space, and $V(\cdot)$ denotes volume.

Local porosity distribution $\mu(\widetilde{\phi}, L)$ provides the probability density of finding a local porosity equal to $\widetilde{\phi}$ when the side-length of measurement cell is set to L. And it is mathematically defined as follows:

$$\mu(\widetilde{\phi}, L) = \frac{1}{n\Delta\widetilde{\phi}} \sum_{\mathbf{r}} \delta(\widetilde{\phi} - \phi_{\mathrm{local}}(\mathbf{r}, L)) \tag{33}$$

where n is the number of placements of the measurement cells $K(\mathbf{r}, L)$, and $\delta(\widetilde{\phi} - \phi_{\mathrm{local}}(\mathbf{r}, L))$ is the Dirac δ function that is defined as follows:

$$\delta(\widetilde{\phi} - \phi_{\mathrm{local}}(\mathbf{r}, L)) = \begin{cases} 1, \text{ if } \ |\widetilde{\phi} - \phi_{\mathrm{local}}(\mathbf{r}, L)| \leq \mathrm{d}\widetilde{\phi}; \\ 0, \text{ otherwise.} \end{cases} \tag{34}$$

where $\mathrm{d}\widetilde{\phi}$ denotes the interval to build the histogram associated with local porosity distribution. Essentially, $\mu(\widetilde{\phi}, L)\mathrm{d}\widetilde{\phi}$ measures the probability of finding a measurement cell with side-length L and local porosity between $\widetilde{\phi}$ and $\widetilde{\phi} + \mathrm{d}\widetilde{\phi}$. Obviously, $\mu(\widetilde{\phi}, L)$ depends on the side-length L of measurement cells, but there is no common rule to determine an optimal value of L for a specific porous medium.

Local percolation probabilities

Local percolation probabilities (Hilfer, 2002) are used to characterize the connectivity of measurement cells $K(\mathbf{r}, L)$ with the specific local porosity value. A measurement cell $K(\mathbf{r}, L)$ is termed percolating in direction α, if there exists at least one pore path lying inside this measurement cell that connects two points on the opposite surfaces perpendicular to this direction. The indicator function of the measurement cell $K(\mathbf{r}, L)$ percolating in direction α is given by

$$\Lambda_\alpha(\mathbf{r}, L) = \begin{cases} 1, \text{ if } K(\mathbf{r}, L) \text{ percolates in the direction } \alpha; \\ 0, \text{ otherwise.} \end{cases} \tag{35}$$

Thus, $\Lambda_x(\mathbf{r}, L) = 1$, $\Lambda_y(\mathbf{r}, L) = 1$ or $\Lambda_z(\mathbf{r}, L) = 1$ indicates the measurement cell is percolating in the x-, y- or z-direction respectively. It should be noted that $\Lambda_1(\mathbf{r}, L) = 1$ and $\Lambda_3(\mathbf{r}, L) = 1$ indicate the measurement cell is percolating in at least one of the principal directions and in all the three principal directions, respectively. The local percolating probability $\lambda_\alpha(\widetilde{\phi}, L)$ in the direction α is defined as follows:

$$\lambda_\alpha(\widetilde{\phi}, L) = \frac{\sum_{\mathbf{r}} \Lambda_\alpha(\mathbf{r}, L)\delta(\widetilde{\phi} - \phi_{\text{local}}(\mathbf{r}, L))}{\sum_{\mathbf{r}} \delta(\widetilde{\phi} - \phi_{\text{local}}(\mathbf{r}, L))} \tag{36}$$

Basically, $\lambda_\alpha(\widetilde{\phi}, L)$ provides the fraction of measurement cells with side-length L and local porosity $\widetilde{\phi}$ that are percolating in direction α.

Total fraction of percolating cells

Total fraction of percolating cells $T_\alpha(L)$ (Hilfer, 2002) provides the fraction of all measurement cells $K(\mathbf{r}, L)$ with side-length L that are percolating in the direction α, and it is calculated from the integration over all local porosities:

$$T_\alpha(L) = \int_0^1 \mu(\widetilde{\phi}, L)\lambda_\alpha(\widetilde{\phi}, L)\, \mathrm{d}\widetilde{\phi} \tag{37}$$

Total fraction of percolating cells $T_\alpha(L)$ quantifies the connectivity characteristic of the pore network system, which is important for modelling transport properties.

References

Anovitz, L. M. and Cole, D. R. (2015). Characterization and analysis of porosity and pore structures. *Reviews in Mineralogy and Geochemistry*, 80(1):61–164.

Berg, C. F. (2016). Fontainebleau 3d models. `http://www.digitalrocksportal.org/projects/57`.

Blunt, M. J., Bijeljic, B., Dong, H., Gharbi, O., Iglauer, S., Mostaghimi, P., Paluszny, A., and Pentland, C. (2013). Pore-scale imaging and modelling. *Advances in Water Resources*, 51:197–216.

Bostanabad, R. (2020). Reconstruction of 3d microstructures from 2d images via transfer learning. *Computer-Aided Design*, 128:102906.

Bostanabad, R., Bui, A. T., Xie, W., Apley, D. W., and Chen, W. (2016a). Stochastic microstructure characterization and reconstruction via supervised learning. *Acta Materialia*, 103:89–102.

Bostanabad, R., Chen, W., and Apley, D. (2016b). Characterization and reconstruction of 3d stochastic microstructures via supervised learning. *Journal of Microscopy*, 264(3):282–297.

Bultreys, T., De Boever, W., and Cnudde, V. (2016). Imaging and image-based fluid transport modeling at the pore scale in geological materials: A practical introduction to the current state-of-the-art. *Earth-Science Reviews*, 155:93–128.

Buscombe, D. (2008). Estimation of grain-size distributions and associated parameters from digital images of sediment. *Sedimentary Geology*, 210(1-2):1–10.

Cang, R., Xu, Y., Chen, S., Liu, Y., Jiao, Y., and Ren, M. Y. (2017). Microstructure representation and reconstruction of heterogeneous materials via deep belief network for computational material design. *Journal of Mechanical Design*, 139(7):071404.

Choubineh, A., Helalizadeh, A., and Wood, D. A. (2019). Estimation of minimum miscibility pressure of varied gas compositions and reservoir crude oil over a wide range of conditions using an artificial neural network model. *Advances in Geo-Energy Research*, 3(1):52–66.

Corson, P. B. (1974). Correlation functions for predicting properties of heterogeneous materials. ii. empirical construction of spatial correlation functions for two-phase solids. *Journal of Applied Physics*, 45(7):3165–3170.

Cui, S., Fu, J., Cen, S., Thomas, H. R., and Li, C. (2021). The correlation between statistical descriptors of heterogeneous materials. *Computer Methods in Applied Mechanics and Engineering*, 384:113948.

Dong, H. (2008). *Micro-CT imaging and pore network extraction*. PhD thesis, Department of Earth Science and Engineering, Imperial College London.

Farrell, N. and Healy, D. (2017). Anisotropic pore fabrics in faulted porous sandstones. *Journal of Structural Geology*, 104:125–141.

Feng, J., Cen, S., Li, C., and Owen, D. (2016). Statistical reconstruction and karhunen–loève expansion for multiphase random media. *International Journal for Numerical Methods in Engineering*, 105(1):3–32.

Feng, J., Li, C., Cen, S., and Owen, D. (2014). Statistical reconstruction of two-phase random media. *Computers & Structures*, 137:78–92.

Feng, J., Teng, Q., Li, B., He, X., Chen, H., and Li, Y. (2020). An end-to-end three-dimensional reconstruction framework of porous media from a single two-dimensional image based on deep learning. *Computer Methods in Applied Mechanics and Engineering*, 368:113043.

Fu, J., Cui, S., Cen, S., and Li, C. (2021a). Statistical characterization and reconstruction of heterogeneous microstructures using deep neural network. *Computer Methods in Applied Mechanics and Engineering*, 373:113516.

Fu, J., Dong, J., Wang, Y., Ju, Y., Owen, D. R. J., and Li, C. (2020a). Resolution effect: An error correction model for intrinsic permeability of porous media estimated from lattice boltzmann method. *Transport in Porous Media*, 132(3):627–656.

Fu, J., Li, D., Thomas, H. R., and Li, C. (2021b). Permeability prediction for natural porous rocks through feature selection and machine learning. *Under Review*.

Fu, J., Thomas, H. R., and Li, C. (2020b). Tortuosity of porous media: Image analysis and physical simulation. *Earth-Science Reviews*, page 103439.

Gao, Q.-F., Jrad, M., Hattab, M., Fleureau, J.-M., and Ameur, L. I. (2020). Pore morphology, porosity, and pore size distribution in kaolinitic remolded clays under triaxial loading. *International Journal of Geomechanics*, 20(6):04020057.

Golparvar, A., Zhou, Y., Wu, K., Ma, J., and Yu, Z. (2018). A comprehensive review of pore scale modeling methodologies for multiphase flow in porous media. *Advances in Geo-Energy Research*, 2(4):418–440.

Hajizadeh, A., Safekordi, A., and Farhadpour, F. A. (2011). A multiple-point statistics algorithm for 3d pore space reconstruction from 2d images. *Advances in Water Resources*, 34(10):1256–1267.

Herring, A., Sheppard, A., Turner, M., and Beeching, L. (2018). Multiphase flows in sandstones. `http://www.digitalrocksportal.org/projects/135`.

Hilfer, R. (2002). Review on scale dependent characterization of the microstructure of porous media. *Transport in Porous Media*, 46(2-3):373–390.

Ijeje, J. J., Gan, Q., and Cai, J. (2019). Influence of permeability anisotropy on heat transfer and permeability evolution in geothermal reservoir. *Advances in Geo-Energy Research*.

Ju, Y., Zheng, J., Epstein, M., Sudak, L., Wang, J., and Zhao, X. (2014). 3d numerical reconstruction of well-connected porous structure of rock using fractal algorithms. *Computer Methods in Applied Mechanics and Engineering*, 279:212–226.

Karsanina, M. V. and Gerke, K. M. (2018). Hierarchical optimization: Fast and robust multiscale stochastic reconstructions with rescaled correlation functions. *Physical Review Letters*, 121(26):265501.

Kotsiantis, S. B., Zaharakis, I., and Pintelas, P. (2007). Supervised machine learning: A review of classification techniques. *Emerging Artificial Intelligence Applications in Computer Engineering*, 160:3–24.

Latief, F., Biswal, B., Fauzi, U., and Hilfer, R. (2010). Continuum reconstruction of the pore scale microstructure for fontainebleau sandstone. *Physica A: Statistical Mechanics and its Applications*, 389(8):1607–1618.

Li, S. Z. (2009). *Markov random field modeling in image analysis*. Springer Science & Business Media.

Li, X., Liu, Z., Cui, S., Luo, C., Li, C., and Zhuang, Z. (2019). Predicting the effective mechanical property of heterogeneous materials by image based modeling and deep learning. *Computer Methods in Applied Mechanics and Engineering*, 347:735–753.

Li, X., Zhang, Y., Zhao, H., Burkhart, C., Brinson, L. C., and Chen, W. (2018). A transfer learning approach for microstructure reconstruction and structure-property predictions. *Scientific Reports*, 8(1):1–13.

Liang, Z., Fernandes, C., Magnani, F., and Philippi, P. (1998). A reconstruction technique for three-dimensional porous media using image analysis and fourier transforms. *Journal of Petroleum Science and Engineering*, 21(3-4):273–283.

Liu, X. and Shapiro, V. (2015). Random heterogeneous materials via texture synthesis. *Computational Materials Science*, 99:177–189.

Lu, X., Heenan, T. M., Bailey, J. J., Li, T., Li, K., Brett, D. J., and Shearing, P. R. (2017). Correlation between triple phase boundary and the microstructure of solid oxide fuel cell anodes: The role of composition, porosity and ni densification. *Journal of Power Sources*, 365:210–219.

Møller, M. F. (1993). A scaled conjugate gradient algorithm for fast supervised learning. *Neural networks*, 6(4):525–533.

Mosser, L., Dubrule, O., and Blunt, M. J. (2017). Reconstruction of three-dimensional porous media using generative adversarial neural networks. *Physical Review E*, 96(4):043309.

Münch, B. and Holzer, L. (2008). Contradicting geometrical concepts in pore size analysis attained with electron microscopy and mercury intrusion. *Journal of the American Ceramic Society*, 91(12):4059–4067.

Murphy, K. P. (2012). *Machine learning: A probabilistic perspective*. MIT press.

Okabe, H. and Blunt, M. J. (2005). Pore space reconstruction using multiple-point statistics. *Journal of Petroleum Science and Engineering*, 46(1-2):121–137.

Rabbani, A. and Ayatollahi, S. (2015). Comparing three image processing algorithms to estimate the grain-size distribution of porous rocks from binary 2d images and sensitivity analysis of the grain overlapping degree. *Special Topics & Reviews in Porous Media: An International Journal*, 6(1).

Schlüter, S., Sheppard, A., Brown, K., and Wildenschild, D. (2014). Image processing of multiphase images obtained via x-ray microtomography: A review. *Water Resources Research*, 50(4):3615–3639.

Schlüter, S. and Vogel, H.-J. (2011). On the reconstruction of structural and functional properties in random heterogeneous media. *Advances in Water Resources*, 34(2):314–325.

Scrivener, K. L. (2004). Backscattered electron imaging of cementitious microstructures: Understanding and quantification. *Cement and Concrete Composites*, 26(8):935–945.

Shukla, K., Jagtap, A. D., Blackshire, J. L., Sparkman, D., and Karniadakis, G. E. (2021). A physics-informed neural network for quantifying the microstructure properties of polycrystalline nickel using ultrasound data. *arXiv preprint arXiv:2103.14104*.

Soille, P. (2013). *Morphological image analysis: Principles and applications*. Springer Science & Business Media.

Stutzman, P. (2004). Scanning electron microscopy imaging of hydraulic cement microstructure. *Cement and Concrete Composites*, 26(8):957–966.

Sundararaghavan, V. and Zabaras, N. (2005). Classification and reconstruction of three-dimensional microstructures using support vector machines. *Computational Materials Science*, 32(2):223–239.

Tahmasebi, P. and Sahimi, M. (2012). Reconstruction of three-dimensional porous media using a single thin section. *Physical Review E*, 85(6):066709.

Taiwo, O. O., Finegan, D. P., Eastwood, D. S., Fife, J. L., Brown, L. D., Darr, J. A., Lee, P. D., Brett, D. J., and Shearing, P. R. (2016). Comparison of three-dimensional analysis and stereological techniques for quantifying lithium-ion battery electrode microstructures. *Journal of Microscopy*, 263(3):280–292.

Torquato, S. (2002). Statistical description of microstructures. *Annual Review of Materials Research*, 32(1):77–111.

Torquato, S. (2013). *Random heterogeneous materials: Microstructure and macroscopic properties*, volume 16. Springer Science & Business Media.

Torquato, S. and Yeong, C. (1998). Reconstructing random media ii. three-dimensional media from two-dimensional cuts. *Physical Review E*, 58(1):224–233.

Turner, D. M. and Kalidindi, S. R. (2016). Statistical construction of 3-d microstructures from 2-d exemplars collected on oblique sections. *Acta Materialia*, 102:136–148.

Wang, J., Aldosary, M., Cen, S., and Li, C. (2021). Hermite polynomial normal transformation for structural reliability analysis. *Engineering Computations*.

Wang, Y., Arns, C. H., Rahman, S. S., and Arns, J.-Y. (2018). Porous structure reconstruction using convolutional neural networks. *Mathematical Geosciences*, 50(7):781–799.

Wei, L. and Levoy, M. (2000). Fast texture synthesis using tree-structured vector quantization. In *Proceedings of the 27th Annual Conference on Computer Graphics and Interactive Techniques*, pages 479–488. ACM Press/Addison-Wesley Publishing Co.

Wood, D. A. (2018). A transparent open-box learning network provides insight to complex systems and a performance benchmark for more-opaque machine learning algorithms. *Advances in Geo-Energy Research*, 2(2):148–162.

Wu, K., Van Dijke, M. I., Couples, G. D., Jiang, Z., Ma, J., Sorbie, K. S., Crawford, J., Young, I., and Zhang, X. (2006). 3d stochastic modelling of heterogeneous porous media–applications to reservoir rocks. *Transport in Porous Media*, 65(3):443–467.

Wu, Y., Lin, C., Ren, L., Yan, W., An, S., Chen, B., Wang, Y., Zhang, X., You, C., and Zhang, Y. (2018). Reconstruction of 3d porous media using multiple-point statistics based on a 3d training image. *Journal of Natural Gas Science and Engineering*, 51:129–140.

Yang, M., Nagarajan, A., Liang, B., and Soghrati, S. (2018). New algorithms for virtual reconstruction of heterogeneous microstructures. *Computer Methods in Applied Mechanics and Engineering*, 338:275–298.

Yang, Z., Yu, C.-H., and Buehler, M. J. (2021). Deep learning model to predict complex stress and strain fields in hierarchical composites. *Science Advances*, 7(15):eabd7416.

Yegnanarayana, B. (2009). *Artificial neural networks*. PHI Learning Pvt. Ltd.

Yeong, C. and Torquato, S. (1998). Reconstructing random media. ii. three-dimensional media from two-dimensional cuts. *Physical Review E*, 58(1):224.

Zhang, F., Teng, Q., Chen, H., He, X., and Dong, X. (2021). Slice-to-voxel stochastic reconstructions on porous media with hybrid deep generative model. *Computational Materials Science*, 186:110018.